Politecnico di Torino

Politecnico di Torino

Department of Energy (DENERG)
Master of Science in Renewable Energy Systems
July 2025

Advanced Solvents for Mineral Dissolution and CO_2 Capture Application

Supervisors

Professor Sergio Bocchini
Anna Vittoria De Napoli
Mattia Bartoli, Ph.D.

Candidate

Ardalan Fallah Safsari

Abstract

The rising concentration of atmospheric CO_2 poses a serious threat to global ecosystems, requiring the development of sustainable and efficient carbon capture and storage (CCS) strategies. This thesis investigates the potential of choline-based amino acid ionic liquids (ChoAAILs) as environmentally friendly solvents for CO_2 capture and mineral dissolution processes. Two ionic liquids—choline prolinate ([Cho][Pro]) and choline lysinate ([Cho][Lys])—were synthesized via metathesis reactions and characterized through ATR-IR, TGA-IR, XRD, and Raman spectroscopy.

Experimental analyses revealed that [Cho][Lys] significantly enhanced the dissolution of olivine (Mg_2SiO_4) and facilitated the formation of magnesium carbonate hydrates under mild carbonation conditions (25–50 °C, 1–5 bar CO_2). X-ray diffraction confirmed the precipitation of carbonate phases, while Raman spectra highlighted vibrational shifts associated with CO_2 uptake. TGA-IR analyses indicated thermal stability for both ILs up to approximately 185°. These findings suggest the suitability of ChoAAILs for CCS applications under relatively low-energy conditions.

In addition, computational simulations using HyperChem were conducted to evaluate the reaction kinetics. The activation energy for olivine dissolution was reduced from 25.21 to 11.81 kcal/mol upon CO_2 introduction, confirming its catalytic role in enhancing mineral reactivity.

Overall, the study demonstrates that choline-based amino acid ionic liquids, especially [Cho][Lys], represent promising alternatives to conventional solvents due to their low toxicity, biodegradability, and tunable physicochemical properties. The synergy between ILs and CO_2 opens new opportunities for scalable mineral carbonation routes, aligning with green chemistry principles and offering potential for integration into industrial CCS technologies.

Table of Contents

Abbreviations

AA Amino Acid

AAILs Amino Acid-based Ionic Liquids

ATR-IR Attenuated Total Reflection Infrared

BBILs Bio-based Ionic Liquids

[Cho][Pro] Choline Proline

[Cho][Lys] Choline Lysine

ChILs Cholinium based Ionic Liquids

ChAAIL Choline-Amino Acid based Ionic Liquids

DMSO Dimethyl Sulfoxide

FT-IR Fourier-Transform Infrared

IIT Italian Institute of Technology

IL Ionic Liquid

IR Infrared

MEA Monoethanolamine

TGA Thermogravimetric analysis

XRD X-ray diffraction

BET Brunauer, Emmett and Teller

QAC Quaternary ammonium compound

PCC Post-combustion CO_2 capture

CCS Carbon capture and storage

TEA Triethylamine

MDEA Methyldiethanolamine

PT Proton transfer

ChoCl Choline Chloride

CCD Charge-coupled device

SERS Surface-enhanced Raman Spectroscopy

HMI Human-machine interface

MM Molecular mechanics

ZINDO/1 Zerner's Intermediate Neglect Differential Overlap version 1

AM1 Austin Model 1

PM 3 Parametric Method 3

MD Molecular dynamics

DTG Derivative thermogravimetric

EG Ethylene glycol

Chapter 1

Introduction

1.1 CO_2 problem

Human society today faces an escalating challenge: the steady and persistent accumulation of carbon in the Earth's atmosphere. This issue stems largely from the continuous burning of fossil fuels, widespread deforestation, industrial activities, and other human-driven processes that release vast amounts of carbon dioxide. Unlike sudden disasters, this build-up happens gradually, quietly altering the balance of the natural world. Rising atmospheric CO_2 levels have far-reaching impacts, disrupting rainfall patterns, warming oceans, and reshaping the landscapes we inhabit. These changes are interconnected, revealing how no part of the planet exists in isolation. What happens in one area can quickly ripple across others, much like the steady increase in atmospheric CO_2 affects ecosystems and societies globally.

One of the most visible consequences is the progressive warming of the planet. Carbon dioxide traps heat by preventing infrared radiation from escaping into space, leading to a continuous rise in land and ocean temperatures. The oceans are now absorbing heat more rapidly than in the past, causing them to expand and accelerating the melting of polar ice caps. Together, these effects contribute to more aggressive coastal erosion and flooding. Places once considered safe from the sea are now slowly being reclaimed by advancing waters, reshaping familiar coastlines and forcing long-established communities to abandon their homes.

This warming also drives more intense rainfall and storms. Warmer air holds more moisture, which fuels stronger hurricanes, typhoons, and extreme weather events. These storms not only cause widespread destruction to infrastructure but also erode natural coastal defenses, such as mangroves, salt marshes, and wetlands. These fragile ecosystems act as buffers, softening the impact of waves and storms and offering critical protection to inland regions. As these natural barriers are lost, coastal communities become increasingly vulnerable to the twin threats of flooding and erosion. The collapse of these ecosystems also puts the livelihoods and food security of dependent populations at risk. As temperatures continue to rise, many regions are experiencing longer, more

intense heatwaves. This heat influences rainfall patterns, causing some areas to suffer prolonged droughts while others face severe flooding. In places where occasional rain once supported agriculture, long dry spells now crack the soil and leave fields barren. Conversely, heavy downpours in other regions wash away the fertile topsoil essential for farming. This unpredictable combination of drought and deluge is destabilizing food production systems, with too little water in some areas and destructive excess in others. Although higher CO_2 levels can sometimes promote faster plant growth, this advantage often comes with a trade-off: reduced nutritional quality of the crops. Many agricultural zones now face a precarious balance, as crops struggle to survive under extreme heat, damaging droughts, and sudden floods that strip the land of its vital nutrients.

In the face of these shifting environmental pressures, agriculture worldwide is becoming increasingly unreliable, threatening both food availability and long-term sustainability. While CO_2-driven growth might seem beneficial on the surface, the harsher growing conditions, lower food quality, and frequent disruptions are painting a far more complex and concerning picture for the future of global food security [1].

Water is fundamental to all life, yet it too is deeply affected by the growing impacts of climate change. The natural balance that governs how water moves—from lakes and rivers to underground aquifers—is being steadily disrupted by the warming of the planet. In many parts of the world, people now face two opposite but equally difficult problems: some regions suffer from prolonged droughts and shrinking water supplies, while others are overwhelmed by sudden, heavy rainfall that leads to destructive flooding. This growing unpredictability makes it harder for communities to plan for the future and severely complicates agricultural activities, which are essential for feeding the global population. In addition, crucial freshwater sources like glaciers and mountain snowpacks are retreating at alarming rates. As these natural water reservoirs melt, millions of people find themselves with less and less dependable access to water, particularly during dry seasons when these reserves were once critical safety nets.

The rising concentration of carbon dioxide contributes to a broad array of worsening problems, affecting nearly all forms of life on Earth. Every living organism depends on the stability of its surroundings, and as this stability weakens, biodiversity itself is placed at risk. In the oceans, coral reefs—vital, vibrant ecosystems teeming with life—are among the most vulnerable. As waters warm, these reefs lose their color and their capacity to support marine species. On land, the story is much the same: forests, especially tropical and subtropical ones, are increasingly threatened by relentless droughts and widespread, persistent wildfires. As these habitats shrink and become fragmented, many species struggle to survive, some nearing extinction. The loss of biodiversity is not merely a loss of nature’s

beauty, it also strips away the essential services ecosystems provide, from purifying water and supporting agriculture through pollination to regulating climate patterns.
The wide, ranging consequences we now face, rising seas, stronger storms, shifting rainfall patterns, collapsing crops, vanishing water sources, and the ongoing disappearance of countless species and habitats—are all interconnected, tied to the relentless emission of CO_2 into the atmosphere. This creates a complex chain of reactions where one issue fuels another, forming feedback loops that are increasingly difficult to break. Human-driven practices, especially those tied to energy generation, food production, and land management, are pushing natural systems toward dangerous tipping points. Without significant changes, these practices will prove unsustainable, threatening the long-term balance upon which both nature and human societies depend [2].
Successfully tackling these pressing challenges requires more than just surface-level solutions; it demands a thorough understanding of their underlying causes. While cutting back on carbon dioxide emissions is a critical step, it is not enough on its own. Alongside efforts to limit future emissions, it is equally important to develop strategies that help us adapt to the changes already unfolding around us. The shifts in climate and environment are well underway, and addressing them calls for flexible, forward-thinking approaches. Although many of the necessary technologies are still emerging and far from being fully realized, they offer promising possibilities. These innovations could play a key role in easing the impact of climate change while supporting the gradual healing and restoration of ecosystems.

1.2 Olivine and dissolution

This introduction provides a broad overview of olivine's reactivity in aqueous environments. Olivine stands out as one of the most extensively studied multi-oxide silicate minerals, having been explored under a wider range of scientific conditions than most comparable minerals. Interestingly, much of the literature in this area shares a common starting point, frequently building on similar foundational studies [3]. Although it may seem expected, the observation of consistent corrosion features on naturally weathered olivines from various geological origins suggests that the mineral tends to weather in a remarkably uniform manner, regardless of the specific conditions of its formation or recrystallization. This indicates that olivine's reactivity appears to follow consistent trends across different experimental setups, a characteristic that sets it apart from many other minerals, whose dissolution behaviors often show greater variability [4].
Another key reason for investigating olivine's dissolution is the relative simplicity of its structure. Olivine is composed of isolated SiO_4^{4-} tetrahedra

connected by divalent metal cations, forming a straightforward crystalline framework. This makes its dissolution mechanisms less complex than those of other naturally occurring silicates with more intricate bonding networks [5]. Unlike minerals that form extensive silicate sheets or networks, olivine does not develop large leached layers during dissolution because its structure lacks Si-O-Si linkages. This structural feature also supports its relatively fast dissolution at ambient temperatures in aqueous environments. As a result, earlier studies typically focused on olivine dissolution under highly undersaturated conditions, minimizing the risk that solution chemistry would approach equilibrium and thereby slow the reaction rates. This suggests that a targeted investigation of olivine's behavior at room temperature could offer broader insights into the dissolution mechanisms of silicate minerals more generally [3].

Recent research [6], [7] has expanded this understanding by analyzing available datasets to develop predictive models for forsterite dissolution rates based on variables such as pH and temperature. These studies also emphasize the importance of other less tightly controlled factors, including surface area variations and the influence of microbial activity, which can significantly affect dissolution behavior.

The crystalline structure of a mineral is central to its chemical reactivity, as it dictates which atomic bonds must be broken during dissolution and determines the surface features that interact with the surrounding solution. Olivine's structure consists of SiO_4^{4-} tetrahedral anions combined with divalent metal cations Me^{2+} in a 1:2 ratio. These cations are arranged in continuous octahedral chains along the c-axis, a key feature of olivine's framework [8], [9]. A simplified view of the olivine structure along the a-axis is provided in Figure 1. Each silicon atom is covalently bonded to four oxygen atoms, and these oxygen atoms carry a partial negative charge. The divalent metal cations are ionically bonded to the oxygen atoms of the silicate tetrahedra, but the structure lacks bridging Si-O-Si bonds typically found in other silicate minerals. Within the lattice, cations occupy two distinct octahedral sites, labeled M1 and M2. The M2 site is generally larger and more structurally stable than the M1 site [3].

The specific metal cation present in the framework defines the type of olivine. For example, when manganese predominates, the mineral is known as tephroite; with iron, it is fayalite; and with magnesium, it is forsterite. The most abundant olivine on Earth is a magnesium-rich variety that typically contains about 10% Fe^{2+} within its structure. Because of its prevalence, much of the scientific work focuses on this forsterite-dominant composition.

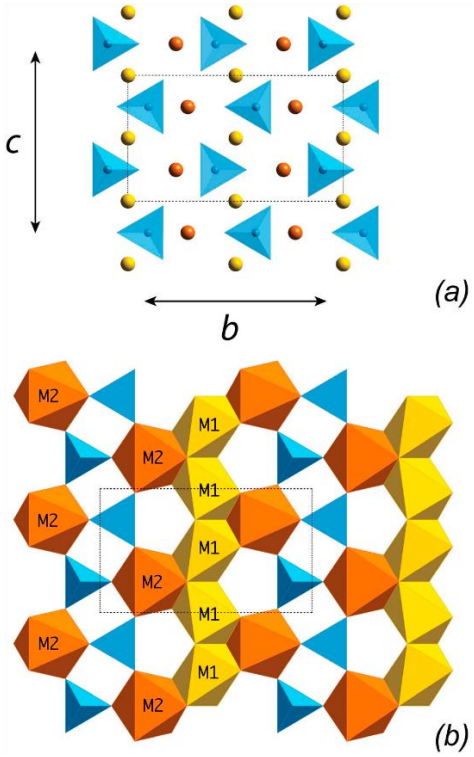

Figure 1: *"Projections of the of olivine (Me_2SiO_4) structure down the a axis of the orthorhombic unit cell (dashed line). (a) Arrangement of two levels of the isolated SiO_4 tetrahedra aligned along the b and c axes and pointing alternately up and down along c; M_1 and M_2 cations are represented by yellow and orange colors, respectively. (b) Geometric distribution and connection of M_1 and M_2 octahedra relative to the SiO_4 tetrahedra on a single level of the unit cell" [3].*

A primary factor governing the dissolution behavior of silicate minerals in aqueous environments is the nature of the atomic bonds that define their internal structure, particularly the silicon-oxygen framework and the types of metal-oxygen interactions present within the mineral lattice [5], [16], [17]. In the case of forsterite, the structure is composed of isolated silicon-oxygen tetrahedra that are connected through magnesium cations. This arrangement allows olivine to dissolve primarily through the disruption of the ionic bonds between magnesium and oxygen, which subsequently releases the silicate anions (SiO_4^{4-}) into solution. Because olivine's structure lacks strong covalent silicon-oxygen-silicon (Si-O-Si) linkages and is instead dominated by relatively weak ionic metal-oxygen bonds, it is classified among silicate minerals that dissolve rapidly in aqueous conditions [18].

The dissolution behavior of olivine is notably different from that of other multi-oxide silicates, which typically require the sequential breaking of several metal-oxygen bonds during dissolution. In such minerals, these bonds tend to break stepwise, often through proton-mediated exchange

reactions that depend on the specific reactivity of each metal site under the given environmental conditions [5]. Consequently, the way olivine dissolves cannot be viewed as fully representative of the broader family of multi-oxide silicate minerals. However, studying its relatively simple dissolution pathway provides valuable insights that contribute to a more comprehensive understanding of silicate dissolution as a whole.

Experimental observations show that as the pH increases, the rate of forsterite dissolution consistently decreases—a trend commonly observed across magnesium silicates [10], [11]. Temperature also plays a critical role in regulating mineral dissolution rates, which typically follow a pattern described by the Arrhenius relationship. This equation, grounded in transition state theory, indicates that the logarithm of the rate constant, kkk, which represents the concentration rate of the activated complex controlling the reaction, generally varies in a near-linear fashion with the inverse of temperature [17]. This temperature dependence helps explain how and why dissolution rates accelerate or decelerate under different thermal conditions.

$$k = A_0 e^{-\frac{E_a}{RT}} \tag{1}$$

E_a denotes the activation energy, while A_0 refers to a temperature invariant pre-exponential factor. It is noteworthy that the rate constant is related to r_+ the forward dissolution rate using the expression:

$$r_+ = kK \prod_i a_i^{n_i} \tag{2}$$

In which n_i is the stoichiometric number of moles of the *i*th species is involved in the process that leads to 1 mol of this activated or precursor complex, whereas K represents the equilibrium constant for the reaction that leads to the activated or precursor complex. However, the temperature dependence of reaction rates has been described by many applications of the Arrhenius equation like so:

$$r = A'_0 e^{-\frac{E'_a}{RT}} \tag{3}$$

E'_a is the apparent activation energy; A'_0 is a temperature-independent pre-exponential component [12]. Hence, it is the temperature fluctuation of the concentration of the activated or predecessor component that makes E_a different from E'_a.

The only factor on which the dissolving rates of forsterite in aqueous solutions with an activity of H_2O around one and containing only Mg, Si, and simple inorganic acids depend is pH. The constant pH dissolution rates of

forsterite would be given by Equation 3 in such a way that the logarithm of dissolution rates would show as a straight line with respect to temperature, on the assumption that the dissolution system was temperature separated and that the enthalpy of the activated complex formation reaction was roughly constant [3].

According to Chen and Brantley, dissolving rates of forsterite were determined using values of 65 °C and $2 < \text{pH} < 5$. They proposed that the apparent activation energy is pH dependent and dependent upon temperature on the change in rates with pH after using their results in comparison with equivalent rates at 25 °C. As their results showed, forsterite dissolution activation energy was increased from 84 kJ/mol to 125 kJ/mol when the pH decreased from 5 to 0 [3].

For the investigation about surface area, an equivalent geometrical interface dimension, or that of a homogenous geometric object such as a sphere or a cube having the same dimension as mineral grains, can constitute the most basic surface area that is used for describing mineral reactivity. One possible alternative is to couple Brunauer, Emmett, and Teller methods with the surface areas determined from inert gas adsorption techniques [13]. This is good because the adsorbing element, such as Kr or N_2, has a dimension comparable to that of H_2O, making this very suitable to replace water when describing mineral surface interaction. The roughness measure is the ratio of BET surface area to that of the geometric surface area and shows how different the actual surface area is from that of a smooth geometric shape of the same dimension. The roughness attributes of olivine, primarily those employed in most experimental investigations, are generally low and vary from 3 to 10 because of the absence of an internal surface region in olivine [14].

Finally, the relationship between biomass as a microbial species and the rates of forsterite dissolution is under extensive research. According to [15], the dissolution rates of Aheim forsterite are not actually affected by the presence of inactive Synechococcus cyanobacteria. While inactive bacteria have been found to do almost nothing in reducing forsterite dissolution rates, other studies demonstrate that active microbes penetrate the dissolution rates of solid forsterite. The researchers explained the inhibition by stating that organic substances coating the olivine surface reduce the area of the mineral directly exposed to the reactive aqueous fluid. Further evidence for the interpretation comes from the findings of [16] that the surfaces of forsterite exposed to the aerobic gram-negative bacteria Pseudomonas reactants rapidly developed a biofilm-like substance that greatly decreased over time dissolution rates at ambient CO_2 partial pressures. Similarly, protobacteria and fungi, mainly Trichocomaceae, were found to lower the dissolving rate of forsterite by an order of magnitude [26]. The microorganisms specifically populated the reactive spots on the olivine surface, reducing the overall dissolving rates,

according to visualization of the mineral exteriors conducted after this nearly five-year investigation. Microorganisms prefer to inhabit these areas because they tend to be places from which they are able to collect valuable nutrients from the dissolving olivine.

1.3 Sustainable ionic liquid applications

Ionic liquids are those salts which have their melting temperature below 100 °C [19],[20]. They consist of both an anion and a cation, such as pyridinium, imidazolium or ammonium, that merge to create very versatile and tailor-made systems. A few of the main cations and anions that are predominantly used in ILs are presented in Figure 2.

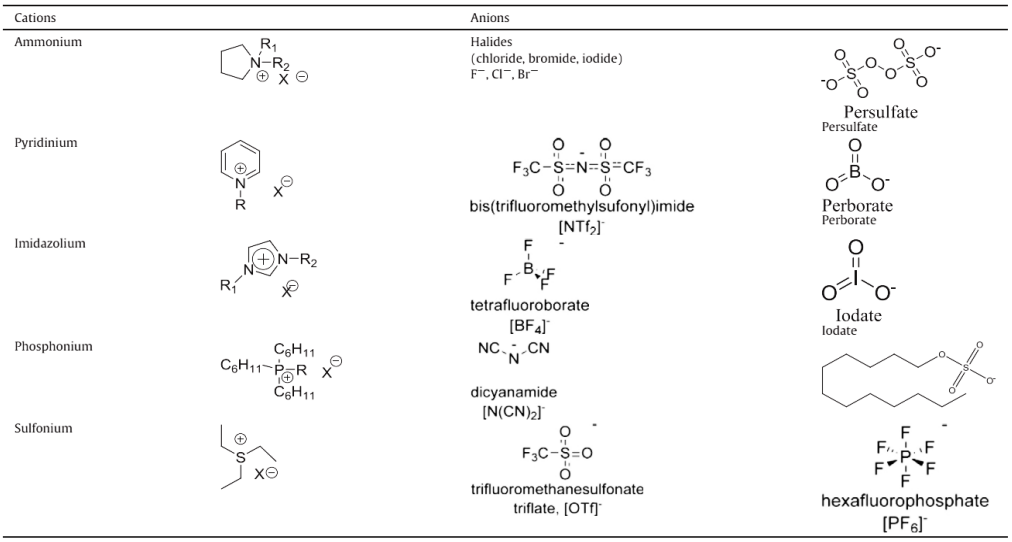

Figure 2: *"Some common cations and anions used in Ils" [21].*

Compared to conventional solvents, ionic liquids (ILs) exhibit exceptionally low vapor pressures, significantly reducing the risk of atmospheric pollution. This characteristic is largely attributed to the strong electrostatic forces between their large, asymmetric cations and anions, which effectively limit their ability to vaporize. As a result, ILs offer clear advantages in processes where minimizing environmental impact and operational hazards is critical, particularly in high-temperature reactions or open-system processes where the evaporation of traditional solvents could pose safety risks.

These unique properties position ionic liquids as promising alternatives to standard solvents in both industrial and laboratory applications, where efficiency and environmental sustainability are increasingly prioritized

[22], [23]. ILs stand out for their distinctive physicochemical features, such as extremely low volatility, excellent thermal stability, and broad solubility ranges for both organic and inorganic compounds, as summarized in Table 1.

Table 1: *General Properties of Ionic Liquids [24].*

Properties of Ionic Liquids	
Vapour pressure	Generally negligible vapour pressure under normal conditions (non-volatile)
Flammability	Usually non-flammable, but some ILs are used as propellants
Number of solvents	$>10^6$ (very high in number)
Tuneability	"Designer solvents" with flexibility of combining cations and anions
Viscosity	Generally high of order 20-97,000 mPa.s
Density	In the range of 0.8-3.3 $g.cm^{-3}$
Refractive Index	In the range of 1.3-2.2
Electrical conductivity	Electrically conducting with conductivity up to 120 $mS.cm^{-1}$
Thermal stability	Generally high thermal stability

The distinctive combination of cations and anions in ionic liquids (ILs) gives rise to a variety of solvation behaviors, which are closely tied to their unique physicochemical properties. These behaviors show considerable variability depending on temperature fluctuations, the specific IL composition, and whether co-solvents are present. Together, these factors influence the complex web of intermolecular forces at play, particularly the formation and disruption of hydrogen bonds [25], [22].

Thanks to their highly adaptable solubility profiles, ILs have found broad application in green chemistry, including gas separation, liquid-liquid extraction, and as alternative solvents for both chemical and enzymatic processes. Their ability to dissolve a wide spectrum of both polar and non-polar molecules makes them especially valuable in industrial processes as well as laboratory-scale research [27].

Ionic liquids can be broadly categorized based on their chemical structure and intended applications:

- **Room Temperature Ionic Liquids (RTILs):** These ILs remain liquid at or near ambient temperatures and are among the most widely studied. Their low melting points, high chemical stability, and broad solubility make them attractive for many uses. RTILs

typically feature cations such as imidazolium, pyridinium, or quaternary ammonium groups [28].

- **Protic Ionic Liquids (PILs):** PILs are characterized by extensive hydrogen bonding networks that improve ionic conductivity, making them particularly useful in electrochemical systems [29].
- **Task-Specific Ionic Liquids (TSILs):** These are tailored ILs designed with specific functional groups attached to either the cation or the anion to customize their properties for particular applications, such as catalysis, separation processes, or electrochemistry [30].
- **Bio-Based Ionic Liquids (BBILs):** Formulated from renewable, naturally derived, or biocompatible materials, BBILs serve as more sustainable alternatives to conventional ILs. Amino acid-based ionic liquids, for instance, use deprotonated amino acids as anions and cations like choline, aiming for low toxicity and biodegradability [31].

Designing new ILs requires careful selection and pairing of cations and anions, typically achieved through several established synthesis methods [32], [33]:

- **Neutralization:** Combining a strong acid with a weak base can yield ILs, especially PILs, through proton transfer reactions [34].
- **Ion Exchange (Metathesis):** This method produces halide-free ILs by reacting a primary IL with a metal salt, often involving silver or alkali metals [34].
- **Direct Synthesis:** Choline hydroxide is commonly reacted with acids or amino acids to produce choline-based ILs, often under controlled conditions that support biodegradability [21].
- **Quaternization:** This process involves alkylating nitrogen-containing molecules to create quaternary ammonium cations, which are then combined with suitable anions to form the desired IL [35].

Choline-based ionic liquids (ChILs) represent a particularly promising class of green solvents. Derived from choline—a quaternary ammonium compound sourced from renewable feedstocks—ChILs align well with sustainability goals due to their low toxicity, biodegradability, and efficient, low-waste synthesis routes [21]. Choline itself is a critical nutrient essential for human metabolism and has been recognized by the US Institute of Medicine as a dietary requirement. It plays important physiological roles in lipid metabolism, cell membrane signaling, and neurotransmitter synthesis, particularly acetylcholine. Phosphatidylcholine, a key phospholipid in biological membranes, is one of choline's most vital derivatives. Since endogenous synthesis via phosphatidylethanolamine methylation is insufficient to meet daily needs, dietary intake of choline is essential for human health [37].

Amino acids used in IL synthesis are naturally occurring building blocks of proteins. α-Amino acids, distinguished by their central carbon bearing both an amino (-NH_2) and a carboxyl (-COOH) group, typically appear as white crystalline solids that dissolve well in water but poorly in alcohol. All α-amino acids, except glycine (which is achiral), exhibit optical activity due to their chiral centers [38].

Biocompatibility and biodegradability assessments of choline- and amino acid-based ILs have produced promising results [39],[40],[41],[42]. Bio-derived ILs made from amino acids not only contribute to sustainability but also offer catalytic versatility, with functional groups that can fine-tune acidity, chirality, and reactivity. These amino acid-based ILs (AAILs) provide greener alternatives to traditional volatile organic solvents and have demonstrated superior performance in several catalytic reactions [43].

One of the most notable applications of these ILs is in **CO_2 capture**. AAILs effectively absorb CO_2 by forming carbamate species, combining the chemical reactivity of amino acids with the stability of ILs. This approach offers a more environmentally friendly pathway for post-combustion CO_2 capture, in line with green chemistry principles. Given their low toxicity, biodegradability, and efficient CO_2 absorption, ILs provide a scalable, sustainable alternative to traditional amine-based solvents [44],[45].

Among these, **choline lysinate** is particularly promising for industrial CO_2 capture applications. Post-combustion CO_2 capture (PCC) has the advantage of being compatible with existing industrial setups and typically relies on chemical absorption processes. Historically, PCC has employed aqueous amines such as monoethanolamine (MEA), methyldiethanolamine (MDEA), and triethylamine (TEA). However, these conventional solvents are associated with high energy demands, corrosion issues, and susceptibility to oxidative degradation [46], [47].

The CO_2 capture efficiency of ILs, particularly Choline-Amino Acid Ionic Liquids (ChoAAILs), depends heavily on the reactivity of their functional groups toward carbon dioxide. ChoAAILs are promising as biocompatible, highly efficient CO_2 absorbers, thanks to their amine-containing anions, which readily form stable carbamate adducts. Adding water as a co-solvent can further enhance CO_2 capture by reducing viscosity and improving gas diffusion, as water weakens hydrogen bonding networks and facilitates proton transfer pathways that accelerate absorption kinetics [48].

One of the key limitations of ILs in gas capture is their inherently high viscosity, which restricts the diffusion of CO_2 and slows the absorption process. Dilution with suitable co-solvents can reduce viscosity and improve both absorption capacity and mass transport [49], [50].

Dimethyl sulfoxide (DMSO) has been widely used to address viscosity issues due to its high boiling point (189 °C), polar aprotic nature, and favorable solubility characteristics. DMSO significantly lowers IL viscosity

and enhances CO_2 absorption rates. However, DMSO can decompose at elevated temperatures, producing degradation products such as sulfuric acid and other acidic compounds that can accelerate further decomposition through autocatalytic reactions [51].

Ethylene glycol offers a safer, biodegradable, and more IL-compatible alternative to DMSO. Its low volatility and favorable environmental profile make it a suitable co-solvent for CO_2 capture processes, contributing to more sustainable and efficient system designs [52], [53].

1.4 Scope of the Thesis

This thesis explores the potential of choline-based amino acid ionic liquids (ChoAAILs) as sustainable and environmentally friendly solvents for enhancing mineral dissolution and supporting CO_2 capture processes. The work specifically focuses on the synthesis, characterization, and application of two ionic liquids: choline prolinate ([Cho][Pro]) and choline lysinate ([Cho][Lys]). The aim is to investigate their role in promoting the dissolution of olivine, a magnesium-rich silicate mineral, and to assess their efficiency in facilitating subsequent carbonation reactions under mild conditions.

The study is structured to address both the chemical and process perspectives of CO_2 capture through mineral carbonation. The first part is dedicated to the synthesis and thorough characterization of the selected ionic liquids. Techniques such as ATR-IR, TGA-IR, X-ray diffraction (XRD), and Raman spectroscopy are employed to confirm their structural integrity, thermal stability, and chemical behavior.

A key objective of this thesis is to assess the dissolution kinetics of olivine in the presence of [Cho][Lys] aqueous solutions, with and without CO_2 bubbling, across different experimental setups. The impact of CO_2 introduction on olivine dissolution rates is examined under controlled laboratory conditions, considering variations in temperature, CO_2 pressure, and reaction duration. Special attention is given to understanding the role of ionic liquid composition and the synergistic effects of added chloride ions.

Furthermore, this work integrates computational simulations using HyperChem to evaluate the energy profiles of the dissolution reactions, offering a complementary theoretical insight. The activation energies are calculated for both standard dissolution and carbonation-assisted scenarios, enabling a deeper understanding of the catalytic influence of CO_2 in enhancing mineral reactivity.

The scope of the thesis extends beyond fundamental dissolution studies. It also seeks to demonstrate the viability of choline-based ILs as low-toxicity, biodegradable, and tunable alternatives to conventional solvents in carbon capture and storage (CCS) strategies. By coupling experimental

observations with simulation results, this work aims to contribute valuable knowledge toward the development of scalable and energy-efficient CO_2 sequestration pathways that leverage the abundance of natural silicate minerals.

Ultimately, this research aspires to provide a sustainable framework for integrating ionic liquids into mineral carbonation processes, aligning with green chemistry principles and paving the way for their potential application in industrial carbon management systems.

Chapter 2

Experimental

To advance the promising potential of ionic liquids in sustainable solvent research, this experimental work focuses specifically on the synthesis and application of choline-based ionic liquids (ILs) derived from biologically relevant building blocks. Choline's inherent structural compatibility, low toxicity, and minimal environmental footprint make it an ideal candidate for the design of task-specific ILs aimed at improving mineral dissolution and supporting carbon capture processes.

Among the most promising candidates are amino acid-derived ILs such as choline prolinate ([Cho][Pro]) and choline lysinate ([Cho][Lys]). These ILs represent a significant step toward the development of non-toxic, biodegradable, and environmentally friendly solvents. Their low toxicity, biocompatibility, and highly tunable physicochemical properties make them particularly suitable for applications including CO_2 capture, biomass processing, and catalysis.

Lysinate is the anionic form of lysine, an essential amino acid for the human body. In chemical terms, lysinate is the conjugate base of lysine, formed when the carboxyl group (-COOH) loses a proton, resulting in the negatively charged carboxylate ($-COO^-$). The molecular formula of lysine is $C_6H_{14}N_2O_2$, and upon deprotonation, it becomes $C_6H_{13}N_2O_2^-$. This anionic form is stable under physiological pH conditions and readily forms salts with metal ions or organic cations.

Similarly, prolinate is derived from proline, a naturally occurring non-essential amino acid. Like lysinate, prolinate is formed by the deprotonation of the carboxyl group, yielding the anion $C_5H_8NO_2^-$ from the original proline molecule, which has the formula $C_5H_9NO_2$. What sets proline apart from most amino acids is its distinctive cyclic structure: its side chain forms a ring that reconnects to the amine nitrogen, giving proline a rigid, conformationally restricted geometry. This unique structure plays a critical role in protein folding and stability, particularly in collagen.

Both lysinate and prolinate serve as key anions capable of forming ionic liquids with choline. Beyond their chemical roles, these amino acid-based anions contribute to the biocompatibility and biodegradability of the

resulting ILs, aligning with green chemistry principles and supporting sustainable solvent design.

The synthesis of [Cho][Pro] and [Cho][Lys] is relatively straightforward and consistent with environmentally responsible practices. In this study, the ILs were prepared by reacting either proline or lysine with potassium hydroxide in ethanol to form their respective potassium salts. These intermediates were then combined with choline chloride to yield the target ILs. The subsequent steps, including neutralization, solvent purification, and rotary evaporation, followed green chemistry protocols to maximize efficiency and minimize waste. The resulting products were viscous ionic liquids with distinct solvation characteristics.

Detailed synthesis procedures for [Cho][Pro] and [Cho][Lys] are provided in the following section, together with the chemical characterization protocols employed to verify their structural, thermal, and rheological properties. These analyses aim to confirm the suitability of these ILs for a wide range of applications, particularly in green chemistry, electrochemical processes, and biotechnology.

2.1 Synthesis

For the synthesis of [Cho][Pro], 10.72 g (0.19 mol) of potassium hydroxide (KOH in pellets supplied by Sigma-Aldrich, purity 99%) was added to 50 ml of methanol (supplied by Sigma-Aldrich, purity ≥99.8%) in a round-bottom flask (the scale has an instrumental error of ±0.001). Once the KOH is fully dissolved, proline (0.17 mol (Figure 3), supplied by Biosynth, is gradually added. After complete dissolution, the mixture is left overnight at room temperature under stirring (see Figure 4).

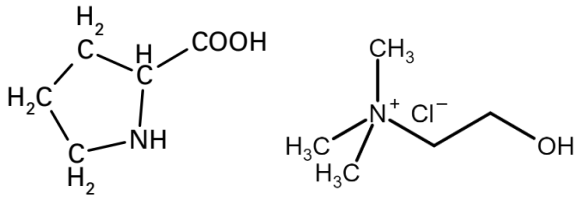

***Figure 3**: Chemical Structure of Proline(left) and Choline Chloride(right) [21].*

Deprotonation of Proline by KOH:

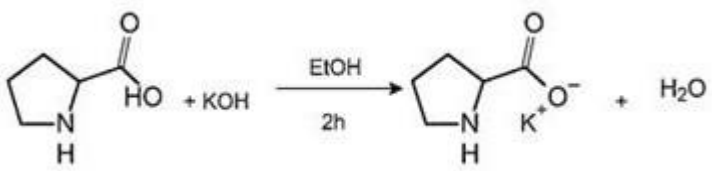

The next day, 0.17 mole of Choline Chloride (ChoCl (Figure 3), supplied by Biosynth, purity 99%), is added, and the mixture is left to mix for 2 hours (see Figure 4).

***Figure 4**: Magnetic stirrer for stirring, producing mixture of [Cho][Pro].*

A solid precipitate of potassium chloride is formed. This precipitation is separated by centrifugation (4200 rpm for 5 min). [Cho][Pro] was produced by rotary evaporation to remove the methanol (see Figure 5). The boiling point for methanol, which should be set, is easily accessible from Table 2. Also, this table is useful for understanding which solvents are miscible or immiscible together.

***Table 2:** Solvent miscibility table.*

SOLVENT MISCIBILITY TABLE

Solvent	Polarity Index	Refractive Index @20˚C	UV(nm) Cutoff @1AU	Boiling Point(˚C)	Viscosity (cPoise)	Solubility in water (%w/w)
Acetic Acid	6.2	1.372	230	118	1.26	100
Acetone	5.1	1.359	330	56	0.32	100
Acetonitrile	5.8	1.344	190	82	0.37	100
Benzene	2.7	1.501	280	80	0.65	0.18
n-Butanol	4.0	1.394	254	125	0.73	0.43
Butyl Acetate	3.9	1.399	215	118	2.98	7.81
Carbon Tetrachloride	1.6	1.466	263	77	0.97	0.08
Chloroform	4.1	1.446	245	61	0.57	0.815
Cyclohexane	0.2	1.426	200	81	1.00	0.01
1,2-Dichloroethane[1]	3.5	1.444	225	84	0.79	0.81
Dichloromethane[2]	3.1	1.424	235	41	0.44	1.6
Dimethylformamide	6.4	1.431	268	155	0.92	100
Dimethyl Sulfoxide[3]	7.2	1.478	268	189	2.00	100
Dioxane	4.8	1.422	215	101	1.54	100
Ethanol	5.2	1.360	210	78	1.20	100
Ethyl Acetate	4.4	1.372	260	77	0.45	8.7
Di-Ethyl Ether	2.8	1.353	220	35	0.32	6.89
Heptane	0.0	1.387	200	98	0.39	0.0003
Hexane	0.0	1.375	200	69	0.33	0.001
Methanol	5.1	1.329	205	65	0.60	100
Methyl-t-Butyl Ether[4]	2.5	1.369	210	55	0.27	4.8
Methyl Ethyl Ketone[5]	4.7	1.379	329	80	0.45	24
Pentane	0.0	1.358	200	36	0.23	0.004
n-Propanol	4.0	1.384	210	97	2.27	100
Iso-Propanol[6]	3.9	1.377	210	82	2.30	100
Di-Iso-Propyl Ether	2.2	1.368	220	68	0.37	
Tetrahydrofuran	4.0	1.407	215	65	0.55	100
Toluene	2.4	1.496	285	111	0.59	0.051
Tichloroethylene	1.0	1.477	273	87	0.57	0.11
Water	9.0	1.333	200	100	1.00	100
Xylene	2.5	1.500	290	139	0.61	0.018

Xylene, Water, Tichloroethylene, Toluene, Tetrahydrofuran, Di-Iso-Propyl Ether, Iso-Propanol, n-Propanol, Pentane, Methyl Ethyl Ketone, Methyl-t-Butyl Ether, Methanol, Hexane, Heptane, Di-Ethyl Ether, Ethyl Acetate, Ethanol, Dioxane, Dimethyl Sulfoxide, Dimethylformamide, Dichloromethane, 1,2-Dichloroethane, Cyclohexane, Chloroform, Carbon Tetrachloride, Butyl Acetate, n-Butanol, Benzene, Acetonitrile, Acetone, Acetic Acid

Immiscible

Miscible

Immiscible means that in some proportions two phases will be produced

Synonym Table
[1] Ethylene Chloride
[2] Methylene Chloride
[3] Methyl Sulfoxide
[4] tert-Butyl Methyl Ether
[5] 2-Butanone
[6] 2-Propanol

***Figure 5**: Rotary evaporator for heating [Cho][Pro], [Cho][Lys] and distilation of solvent.*

This device used a chiller (see Figure 6) for producing -6°C to be sure that all solvent seperates from the main solution.

***Figure 6**: Chiller for producing below zero temperature for distilation of solvent.*

A solution of acetonitrile (supplied by Carlo Erba) and ethanol (9:1 v/v) was added to purify the produced [Cho][Pro] from residual inorganic salts,

which are removed by centrifugation (4200 rpm, 5 min). The solvent is evaporated by rotary evaporation, producing a transparent solution of [Cho][Pro] (see Figure 5).

Metathesis with Choline Chloride:

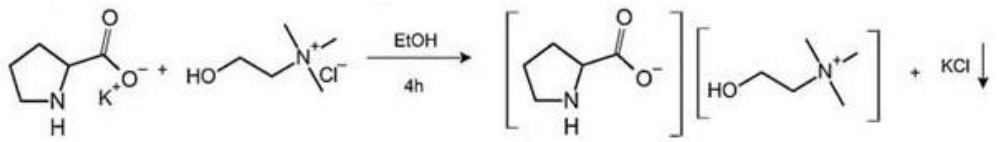

Table 3: *Amount of components to synthesize [Cho][Pro].*

	equivalents	MW (g/mol)	Mole	Quantity	V (ml)
Proline	1	115.13	0.17	20 g	-
Choline Chloride	1	139.62	0.17	24.25 g	-
KOH	1.1	56.10	0.19	10.72 g	-
Methanol	-	-	-	-	50

The choline lisinate [Cho][Lys] was synthesized via ionic metathesis, following a previously reported method for [Cho][Pro]. For the synthesis of [Cho][Lys], 8.44 g (0.15 mol) of potassium hydroxide (KOH in pellets supplied by Sigma-Aldrich, purity 99%) was added to 50 ml of methanol (supplied by Sigma-Aldrich, purity ≥99.8%) in a round-bottom flask (the scale has an instrumental error of ±0.001). Once the KOH is fully dissolved, lysine (0.13 mol (*Figure 7*), supplied by Sigma-Aldrich, purity ≥97%), is gradually added. After complete dissolution, the mixture is left overnight at room temperature under stirring (see Figure 8).

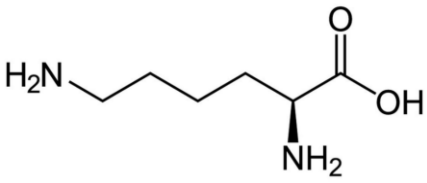

Figure 7*: Chemical Structure of Lysine [21].*

Deprotonation of Lysine by KOH:

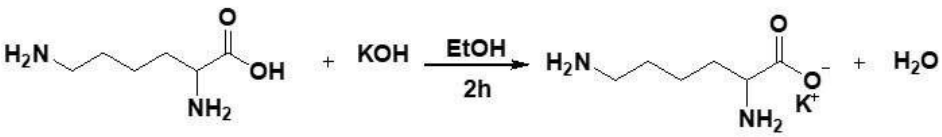

The next day, 0.13 mole of Choline Chloride (ChoCl (Figure 3), supplied by Biosynth, purity 99%) is added, and the mixture is left to mix for 2 hours (see Figure 8).

***Figure 8**: Device for stirring, producing mixture of [Cho][Lys].*

A solid precipitate of potassium chloride is formed. This precipitation is separated by centrifugation (4200 rpm for 5 min). [Cho][Lys] was produced by rotary evaporation to remove the methanol (see Figure 5).
A solution of acetonitrile (supplied by Carlo Erba) and ethanol (9:1 v/v) was added to purify the produced [Cho][Pro] from residual inorganic salts, which are removed by centrifugation (4200 rpm, 5 min). The solvent is evaporated by rotary evaporation, producing a transparent solution of [Cho][Pro].

Metathesis with Choline Chloride:

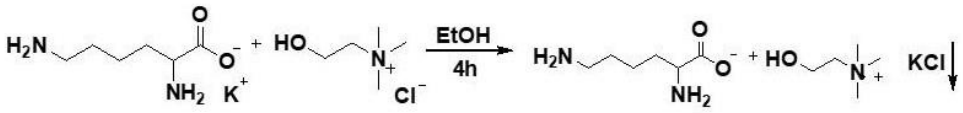

***Table 4:** Amount of components to synthesize [Cho][Lys].*

	equivalents	MW (g/mol)	Mole	Quantity	V (ml)
Lysine	1	146.19	0.13	20 g	-
Choline Chloride	1	139.62	0.13	19.10 g	-
KOH	1.1	56.10	0.15	8.44 g	-
Methanol	-	-	-	-	50

2.2 Olivine and dissolution

This experimental study investigates the dissolution behavior of olivine (Mg_2SiO_4) in the presence of an ionic liquid (IL)-based aqueous medium under varying carbonation conditions. The next goal is evaluating its potential for carbon dioxide (CO_2) capture and sequestration. The approach centers on using a cholinium-lysinate IL, which is composed of the cholinium cation and the deprotonated lysine anion. The reason behind choosing this IL was its sustainability, biocompatibility, and its ability to complex effectively with magnesium ions (Mg^{2+}), the main reactive species in olivine. By performing dissolution of Mg^{2+} from olivine into solution, the IL increases subsequent carbonation reactions and as a potential result, improving the total CO_2 mineralization in effective way.
To evaluate the dissolution kinetics and carbonation behavior, the IL is used at a concentration of 50 wt% in water. Sodium chloride (NaCl) is added to each IL solution in a molar ratio equivalent to the cholinium cation concentration, based on preliminary hypotheses regarding synergistic effects of chloride ions on Mg^{2+} solubilization. Experiments are conducted both under condition without CO_2 insufflation and conditions with continuous CO_2 bubbling. It performed across a range of operational parameters, including reaction temperature, exposure time, and system pressure. This allows for a comprehensive analysis of the influence of carbonation environments on olivine dissolution and carbonate precipitation.
The procedure begins with the preparation of aqueous IL solutions. A 50 wt% cholinium-lysinate solution is prepared using water, resulting in a total solution mass of 10 grams. For each solution, the molar amount of cholinium is calculated based on the approximate molecular weight of cholinium-lysinate (249.35 g/mol). Sodium chloride is then added in a 1:1 molar ratio with respect to the cholinium cation. The solution is stirred thoroughly until the salt dissolves completely.
Olivine granules are prepared by washing with deionized water followed by drying at ambient conditions (see Figure 9).

Figure 9: *Olivine stones.*

The granules are weighed carefully and the moles number of magnesium in the added olivine is equal to the half of cholinium moles present in the solution. the olivine mass required is precisely calculated to maintain stoichiometric balance with the IL by knowing olivine's approximate composition (Mg_2SiO_4) and molecular weight (140.69 g/mol), and assuming Mg content of 34.6 wt%.

When all of them prepared, the olivine granules are added to the IL-water-NaCl solution. Four experimental conditions are examined to assess the role of carbonation:

- Control experiments, conducted in the absence of CO_2 to establish baseline dissolution behavior.
- Carbonation condition 1, involving continuous CO_2 bubbling for 30 minutes at room temperature and ambient pressure (see Figure 10).
- Carbonation condition 2, in which CO_2 is insufflated continuously overnight at 50 °C under ambient pressure (see Figure 10).
- Carbonation condition 3, where the reaction is sustained for one week at 50 °C under a pressurized CO_2 environment of 5 bar using Tecno Delta thermostatized room.

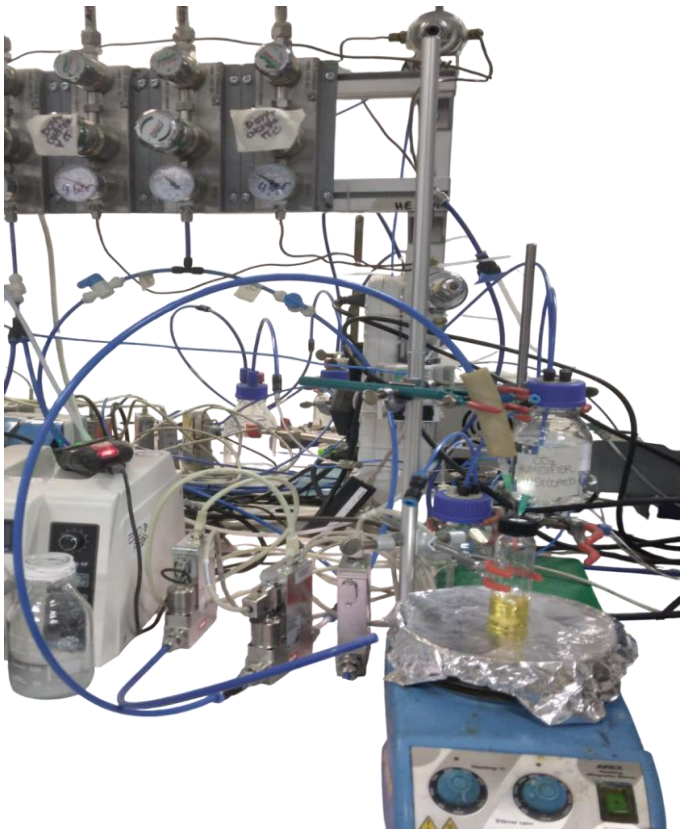

Figure 10: *CO_2 insufflation.*

At the end of the experiment, the liquid and solid phases of each sample are separated. They analyzed for dissolved Mg^{2+} concentration using appropriate spectroscopic methods, which provide a quantitative measure of the olivine dissolution extent. The solid residue is subjected to structural and morphological analysis using X-ray diffraction (XRD) to identify crystalline phases, particularly carbonates, and Raman Spectroscopy to observe surface features and evidence of mineral transformation.
The primary goal of this experiment is to clarify the success of cholinium-lysinate IL, in conjunction with chloride ions and under varying CO_2 bubbling conditions, in enhancing olivine dissolution and promoting the formation of carbonate minerals. Through comparative analysis across the different test environments, the study aims to elucidate both thermodynamic and kinetic factors influencing the reaction pathway. These insights are aimed at participating in the development of sustainable and low-energy mineralization processes for long-term carbon sequestration, particularly those taking advantage of abundant natural silicate minerals such as olivine.
For consistency, 3 experiments are based on a 10 mL solution volume. With the molar mass of cholinium-lysinate (249.35 g/mol), 5 grams of IL correspond to approximately 0.02 mol of cholinium. An equal mass of

water (5 grams) completes the 50 wt% solution. To match the molar concentration of cholinium, 1.17 grams of NaCl is added, calculated from its molar mass (58.44 g/mol). Olivine is added such that the amount of magnesium available for dissolution corresponds to 0.01 mol, i.e., half the amount of cholinium, resulting in approximately 0.70 grams of olivine per test. These calculations ensure that the solution composition is chemically balanced and that the influence of each variable-IL concentration, chloride presence, and CO_2 exposure-can be independently assessed (see Table 5).

Table 5: *Summary table for Control and carbonation condition 1 and 2 experiments.*

[Cho][Lys] 50%	equivalents	MW (g/mol)	m (g)	mol
[Cho][Lys]	1	249.35	5	0.02
Water	14	18	5	0.27
NaCl	1	58.44	1.17	0.02
Mg_2SiO_4	0.5	140.69	0.70	0.01

2.3 Methods

2.3.1 ATR-IR

ATR-IR stands for Attenuated Total Reflectance Infrared Spectroscopy, a qualitative spectroscopic method to determine molecular structure which is used mostly in Fourier Transform Infrared (FTIR) spectroscopy. It is a powerful analytical technique that allows the rapid, non-destructive, and surface analysis of various sample types which is specifically used for the characterization of solids, liquids, pastes, gels, etc., with the least or no sample preparation involved [55]. By performing the infrared spectroscopy with an ATR crystal (commonly made of diamond, zinc selenide, or germanium) together, this allows infrared light to reflect internally within the crystal and generate evanescent waves that penetrate only a few microns into the sample. Selective absorption of certain wavelengths in the IR region corresponding to molecular vibrations generates the absorption spectrum.
In simple terms, the ATR sends waves inside the sample, causing the bonds to vibrate, stretch, or bend. So, every peak in the output corresponds to one kind of vibration and hence one substance. The ATR-IR spectra were collected using a Bruker Tensor II Fourier transform spectrophotometer equipped with a platinum ATR diamond accessory. The IR spectra were recorded at a resolution of 4 cm^{-1}, covering the spectral range from 4000 to 400 cm^{-1}. A total of 128 background scans and 64 sample scans were performed during the analysis. The spectra were subsequently processed using OPUS 8.1® software.

ATR-IR analysis is very advantageous when surface sensitivity is required, making it an excellent technique for the characterization of coatings, thin films, or layered materials. This versatility and efficacy have made it widely useful in several areas, including drugs and excipients identification in pharmaceuticals; material characterization and degradation studies in polymer analysis; fiber or residue detection in forensic investigations; and identification of certain adulterants or contaminants in food analyses.

***Figure 11**: ATR-IR instrument.*

2.3.2 TGA

Thermogravimetric analysis (TGA) is a standard measurement that provides knowledge into thermal stability, decomposition processes, and the compositional time dependent changes of a material under strictly controlled heating conditions. The integration with a Bruker Tensor II Fourier Transform Infrared (FTIR) spectrophotometer equipped with a DTG detector allowed synchronous monitoring of mass loss and evolved gases, thus providing a more complete picture of the sample thermal behavior. Preliminary treatment includes cleaning the instrument with ethanol before placing it inside the ceramic crucible and using gloves to prevent contamination with the actual sample. Empty crucibles are placed in the analyzer and tared on the highly sensitive balance. By pushing the two closing buttons simultaneously, the crucible is isolated and closed.

Around 25 mg of the sample was placed in a crucible for TGA measurements, heated from 30 to 800°C at a slower rate of 10°C.min-1 for better spectral resolution for approximately 48 minutes. Throughout this thermal program, a nitrogen purge gas was flowed inert at 40 mL.min-1 to provide an inert atmosphere and carry any evolved gases to the FTIR system. All thermograms were manipulated using NETZSCH Proteus® software and spectral data analyzed using OPUS 8.1®, thereby allowing for accurate tracking of chemical signatures throughout the thermal event. The TGA is particularly useful for the analysis of complex materials such as polymers, composites, and pharmaceuticals, where thermal stability, chemical composition, and degradation mechanisms are critical for product development, quality control, and failure analysis. The TGA combination provided both precise monitoring of mass loss and in-depth molecular insight into compositional changes and evolution of the decomposition gases, in parallel providing a multiple understanding of the thermal degradation mechanism. During this period, mass changes correlated with thermal events are recorded. The ability to correlate thermal degradation with specific volatile compounds makes TGA a valuable tool for advancing research and ensuring the reliability of materials in various industrial applications.

***Figure 12**: TGA characterization instrument.*

2.3.3 X-ray diffraction (XRD)

A commonly performed analytical way which is known for investigating the crystallographic structure, chemical composition, and physical properties of materials is definitely X-ray diffraction (XRD). Its high accuracy makes it useful in materials science and physics as well as chemistry, geology, and pharmaceutical research. In the study of advanced solvents for olivine dissolution and CO_2 capture, it is critical to understand the structural characteristics of the mineral phases after reaction. X-ray diffraction (XRD) serves as a fundamental tool for characterizing crystalline materials. It enables the identification of mineral composition, changes in phase and crystallinity alterations because of its chemical interaction with solvent systems.

***Figure 13**: X-ray diffraction (XRD) instrument.*

During an XRD experiment, a monochromatic X-ray beam is pointed at the sample. As the X-rays interface with the electrons of atoms in the material, they are scattered elastically. These scattered waves interact with each other. When the path difference between waves meets specific geometric conditions, constructive interference happens. It results in noticeable

diffraction peaks. These peaks provide a fingerprint of the crystal structure [57].
The conditions for constructive interference are described by Bragg's Law, where d is the spacing between atomic planes, θ is the angle of incidence, λ is the X-ray wavelength, and n is an integer representing the order of reflection. Bragg's Law allows for the identification of interlayer distances within the crystal, enabling exact identification of mineral structures and their transformations during reaction processes. This is particularly relevant for assessing changes in minerals after exposure to reactive solvents aimed at CO_2 mineralization or enhanced dissolution [58].

$$2d\sin\theta = n\lambda \quad (4)$$

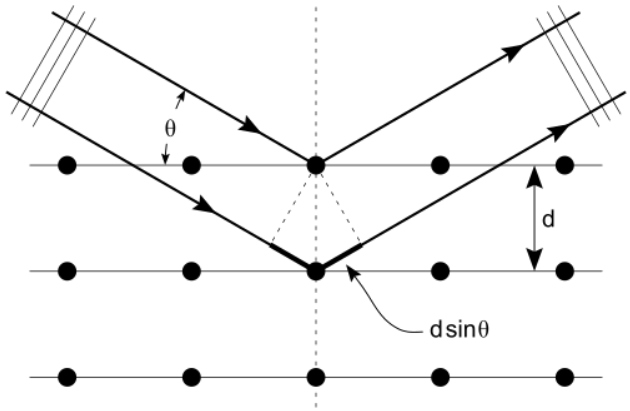

***Figure 14**: Illustration of Bragg's Law.*

The diffraction pattern which is obtained—an intensity plot versus 2θ—contains peaks that correspond to specific crystallographic planes and is typically indexed using Miller indices (h, k, l). From this pattern, important information can be derived, including mineral identity and phase composition, degree of crystallinity and the formation of amorphous products, and crystallite size and microstrain, indicating structural integrity or disorder and phase transitions resulting from solvent–solid interactions.
Because of their interaction with various advanced solvent systems, XRD is used to see the structural change of mineral solids. It helps to verify if carbonate phases form as a result of CO_2 capture or dissolution leads to partial or complete amorphization of the solid phase. Additionally, the technique is important in clarifying intermediate phases that may influence the efficiency or selectivity of the dissolution and carbonation processes.

2.3.4 Raman Spectroscopy

Raman Spectroscopy is an influential evaluative approach adapted to identify and characterize materials according to their exceptional vibrational fingerprints. The method depends on the inelastic scattering of light, recognized as the Raman effect, which gives detailed knowledge about the molecular construction, structure, and physical state of a sample. Primarily, Raman spectroscopy includes highlighting a sample with a monochromatic laser beam. When photons from the laser interface with the molecules in the example, most of them submit to elastic scattering. The scattered photons have the same energy (and thus wavelength) as the incident photons. This process is known as Rayleigh scattering. On the other hand, a small fraction of the incident photons (typically 1 in 10 million) submit to inelastic scattering, which interchanges energy with the molecules and this experience is referred to as Raman scattering.
There are two kinds of Raman scattering: Stokes scattering and Anti-Stokes scattering. In Stokes scattering, the incident photon fails energy to the molecule, promoting it to a raised vibrational energy state. The scattered photon, as a result, has smaller energy and a prolonged wavelength than the incident photon. On the other hand, in Anti-Stokes scattering, the incident photon obtains energy from a molecule that exists in an excited vibrational state which can depart the molecule in a lower energy state. The scattered photon therefore has greater energy and a shorter wavelength than the incident photon. The contrast in energy between the incident and scattered photons is known as the "Raman shift", and it instantly relates to the vibrational energy grades of the molecules within the sample. This move is typically determined by wavenumbers (cm^{-1}) [59], [60].
The Raman spectroscopy device, which has some core elements, is shown in Figure 15. A powerful laser works as the exciting source, giving the monochromatic light needed to cause Raman scattering. The laser beam is focused at the sample, and the scattered light is then gathered and directed into a spectrometer. The light is expanded by the spectrometer, dividing it into its separate wavelengths because of its diffraction grating. Lastly, a detector (such as a CCD camera) records the intensity of the scattered light at different wavelengths. The resulting Raman Spectrum shows the intensity of the scattered light in contrast with the Raman displace (wavenumber), depicting a chain of peaks usual of the sample's molecular vibrations [61], [62].

***Figure 15**: Raman Spectroscopy instrument.*

The thing which works as a specific fingerprint for a particular molecule or material is a singular series of peaks and their alignments in a Raman Spectrum. This specificity makes Raman Spectroscopy an extremely useful tool across various fields. In chemistry, it's suitable for compound identification, purity assessment, and reaction monitoring. In materials science, it helps in characterizing polymers, semiconductors, and nanomaterials. Its non-destructive type and minimal sample processing requirements also make it ideal for biological and biomedical applications involving cell analysis, tissue diagnostics, and drug discovery, even enabling non-invasive glucose sensing. In addition, recent advancements have contributed to techniques similar to surface-enhanced Raman Spectroscopy (SERS), which considerably amplify the Raman signal, opening up possibilities for trace analysis and single-molecule detection [63].

2.3.5 Tecno Delta thermostatized room

This experiment consists of a thermostatically controlled chamber together with a multi-functional testing system. It is designed to investigate gas absorption phenomena under controlled thermal and pressure conditions. The core of the system is an oven fitted with two independent electrical heating elements and a closed-loop refrigeration circuit that employs R134a as the working fluid, enabling precise thermal regulation over a wide temperature range. One of the test reactors is equipped with a magnetic drive agitator in order to help proper mixing of the gas-liquid phases during experiments.

The gas distribution infrastructure is supported by a dedicated panel that includes multiple pressure transmitters for continuous monitoring of system pressures. The instrument related to gas consists of three stainless steel storage cylinders. Each of them has a capacity of 500 mL, which serves as a reservoir for the sample gases. Additionally, two 50 mL reactors are housed within the thermostatic chamber—one equipped with a mixer and the other without—to allow for comparative studies. The entire system is managed and automated via an electrical control panel, which supervises the heating and cooling cycles, thermostats the chamber according to a set point, and continuously monitors pressures in all connected tanks. A schematic diagram of the complete system is provided in Figure 16.

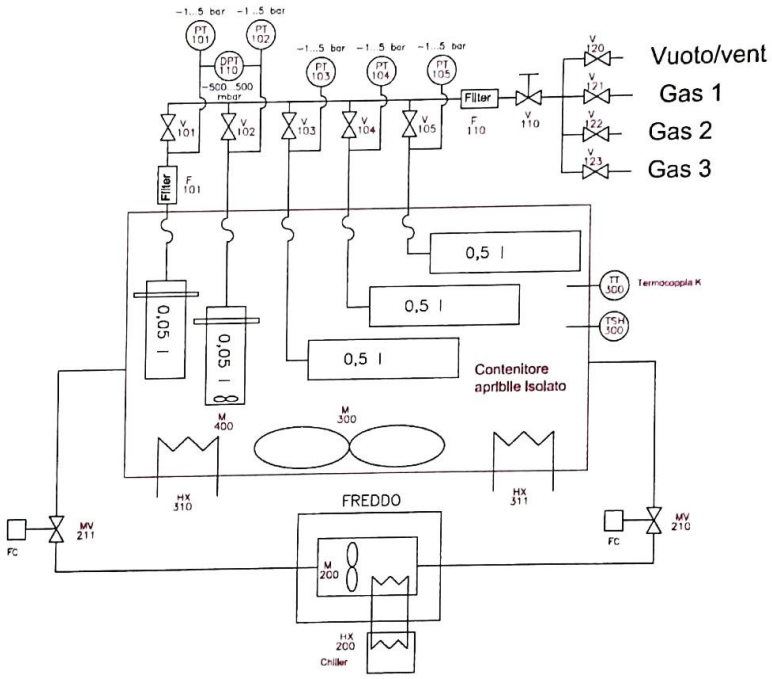

***Figure 16**: Tecno Delta thermostatized room diagram.*

The front control panel is designed for the operator and has a user-friendly interface for system operation. A white indicator light signals the presence of electrical power, while a series of selectors allow the user to choose the operating mode—either heating or cooling—activate the magnetic agitator, and initiate or terminate data acquisition. Two additional buttons are designated for starting and stopping the test cycle, respectively. In the interest of safety, the panel also has an emergency stop button that immediately cuts power to all auxiliary controls. Alarm conditions are indicated by a pulsating signal light, which requires operator acknowledgement. A designed human-machine interface (HMI) screen

enables direct interaction between the operator and the system for monitoring and control (see Figure 17).

***Figure 17**: Control panel of Tecno Delta thermostatized room.*

The primary function of the system is to conduct thermal tests on gas-liquid mixtures under isothermal conditions. A TT300 probe, located inside the oven, serves as the reference sensor for temperature regulation. The thermostatic chamber can provide stable internal temperatures in the range of 10 °C to 120 °C. The system can do experiments in both heating and cooling modes, which depend on the thermal requirements of the specific study.

The valve panel is divided into two main sections: one is used for gas and vacuum supply, and the other is for the distribution of gas into the storage and test tanks. The gas and vacuum supply section has four primary valves (V120, V121, V122, and V123) that enable connection to technical gas sources and vacuum systems. At the below part of these valves, a needle valve (V110) is used to control the rate of gas flow into the tanks. It can also be used to ensure controlled pressurization to the desired set point (see Figure 18).

***Figure 18**: Gas and vacuum supply valve panel.*

Before entering the storage tanks, the gas passes through a filtration unit (F110) with a nominal pore size of 7 microns to remove particulates. Valves V103, V104, and V105 lead the filtered gas into the three 500 mL storage cylinders. Additionally, valves V101 and V102 control the transfer of gas into the two 50 mL reactors—V101 for the reactor with the magnetic mixer and V102 for the non-agitated reactor. To maintain the quality and consistency of the test fluid in the agitated tank, an inline filter (F101) with the same 7-micron rating is included. Each tank is equipped with a pressure transmitter capable of measuring over a range of -1 to 5 barg. Both 50 mL reactors have pressure sensors that help the detection of pressure changes. This is essential for analyzing gas absorption dynamics with high resolution (see Figure 19).

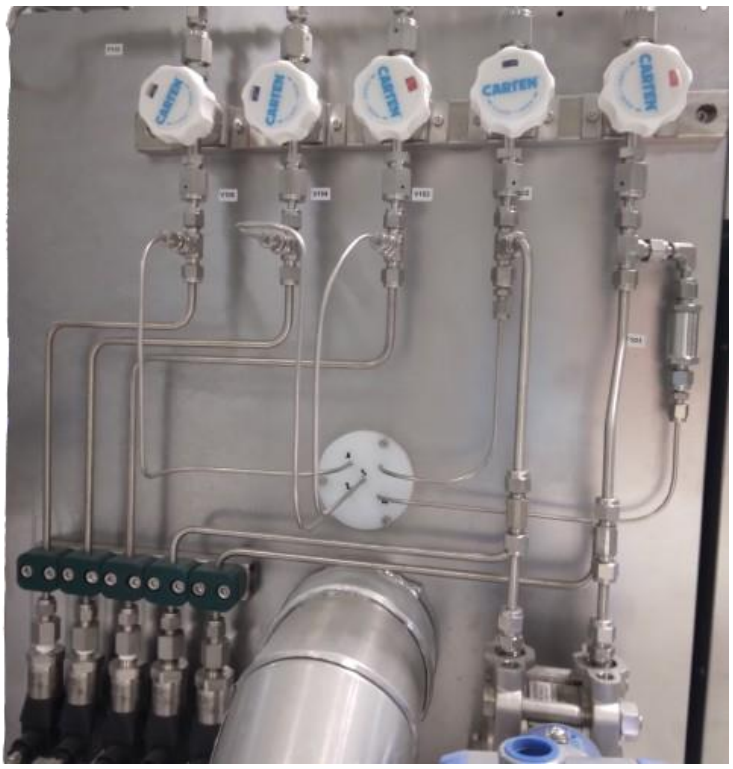

***Figure 19**: Distribution valve panel.*

Inside the thermostatic chamber, the three 500 mL tanks are installed at the back. They can be used when controlled reservoirs containing a known quantity of gas at a fixed pressure are needed. These tanks serve as source vessels for transferring gas into the smaller 50 mL reactors, allowing for precise dosing during the test cycle (see Figure 20).

***Figure 20**: Reactor.*

The agitated reactor is filled with a measured amount of absorbing liquid. The next stage is introducing gas under controlled conditions to study the

kinetics and extent of absorption. The second reactor without agitation can be used as a reference vessel to monitor baseline pressure changes and enable accurate differential analysis between stirred and unstirred conditions. The connection between all vessels is achieved using 1/8-inch capillary tubing with double ferrule compression fittings, which provide secure and serviceable connections suitable for high-precision applications (see Figure 21).

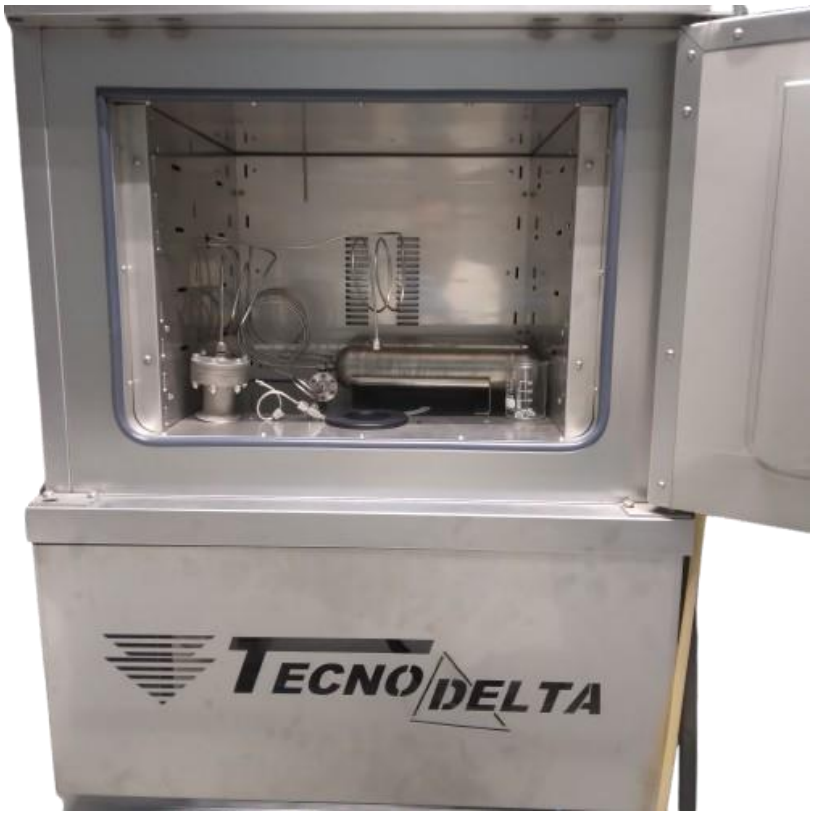

***Figure 21**: Tecno Delta thermostatic chamber.*

The system supports both heating and cooling operations. During heating, the homogenization fan and electrical resistances are activated. The side valves of the chamber remain closed to isolate the heating zone from the refrigeration circuit. The fan operates continuously to confirm a uniform temperature distribution within the chamber. At the same time, the heating elements are controlled via a static relay to adjust power delivery according to the required temperature. For the cooling, particularly at temperatures below 40 °C, a ventilation duct is located at the back part of the chamber. It can be opened to help the refrigeration unit in managing the target temperature.

The test procedure follows a specific sequence to ensure repeatability and accuracy. Initially, the chamber is thermostated to the desired set point of

50 °C, using the TT300 probe for feedback control. 25 mL of the reactor designated for testing is then filled with the sample outside the chamber. After insertion into the chamber, all tanks are evacuated using an external vacuum pump connected via valve V120. Subsequently, the 500 mL storage tanks are charged with carbon dioxide to a pressure of 5 bar by opening valves V103, V104, and V105. The gas is then transferred into the 50 mL reactors through valves V101 and V102, depending on whether agitation is required. In this process, temperature and pressure are continuously watched. It is important that, for safety reasons, the chamber door may only be opened when the test cycle has ended and the internal temperature has decreased under 80 °C.

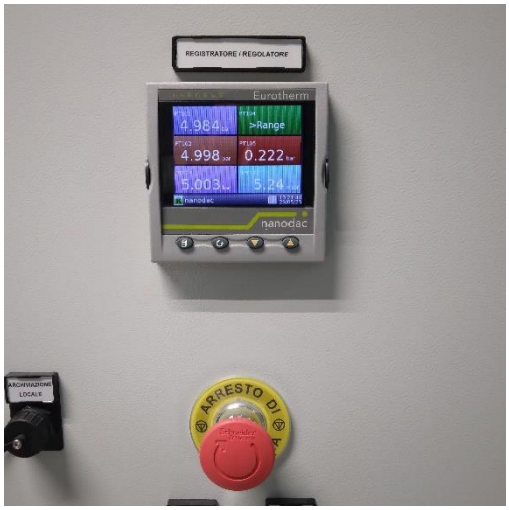

***Figure 22**: Control panel pressure representation.*

With such a design, the temperature and pressure of the tested gases are controlled with precision, detailing how the gases are absorbed into the liquid under various controlled experimental factors. The modular configuration of the setup, meanwhile, along with the control and monitoring ability in real time, offers the flexibility required for basic research and applied testing into gas-liquid interactions.

2.3.6 Simulation

HyperChem is molecular modelling and computational chemistry software developed by Hypercube, Inc. It is designed to combine a graphical user interface with powerful computational tools for the visualization. It is proper for modelling molecular structures, calculating properties, and simulating chemical reactions.
One of the key benefits of HyperChem is the flexibility. It offers a range of computational methods, including molecular mechanics (MM) and semi-

empirical quantum chemistry (such as ZINDO/1, AM1, and PM3). This capability is helpful for users to balance accuracy and computation by the complexity of the system.

The software provides real-time molecular visualization, enabling researchers to construct and manipulate molecules interactively, observe conformational changes, and analyze orbital shapes, charge distributions, and vibrational modes. Its visual interface enables dynamic simulations, for example, molecular dynamics (MD) and geometry optimizations, which are vital for understanding molecular behavior over time and during reactions. HyperChem is valuable in both educational and research fields where flexibility and visualization are important. It is capable of simulating reaction pathways and calculating energy profiles. It is used in studies of molecular structure, reaction mechanisms, thermodynamic properties, and electronic behavior. So HyperChem is suitable for estimating activation energies and analyzing how different environmental or chemical conditions affect molecular interactions. It offers the ability to explore chemical phenomena at the molecular level, whether it is qualitative insight or quantitative accuracy.

Activation energy (E_a) is the minimum energy required for a chemical reaction to occur. In computational chemistry, this is often calculated as:

$$E_a = E_T - E_{Reagents} \tag{5}$$

E_T: Total energy means energy computed for the all reagents in the same structure. In HyperChem, this includes all relevant energy terms (electronic, nuclear repulsion, etc.).

$E_{Reagents}$: Energy of the reagents means the total energy of the reactant molecules before the reaction takes place.

The computational analysis in HyperChem follows a two-phase approach. First, do individual component optimization and then complete system simulation. Initial geometry optimization was performed for each reactant species separately, including choline cation, lysinate anion, sodium chloride (NaCl), water (H_2O), and olivine mineral. Two distinct experimental conditions were modelled: control systems without CO_2 insufflation and carbonation test systems incorporating CO_2. For each component, geometry optimization was conducted independently, and the corresponding optimized total energies were calculated and subsequently summed to determine the total energy of separated reactants ($E_{Reagents}$). Following that, all reagents should be combined within a single molecular structure for comprehensive system analysis. This performs in both control and carbonation test configurations. The calculations employed a hierarchical computational approach, beginning with molecular mechanics (MM) methods followed by semi-empirical techniques to ensure accurate representation of molecular interactions while maintaining computational

efficiency. Energy values were obtained by the HyperChem reach with the compute menu, selecting the properties option, and extracting energy data from the output log. The software reports energy values in (kcal/mol), with both the total energy of system (E_T) and individual reactant energies ($E_{Reagents}$) systematically recorded for next activation energy calculations. All calculations were performed within the HyperChem computational chemistry environment, as illustrated in the figure 23.

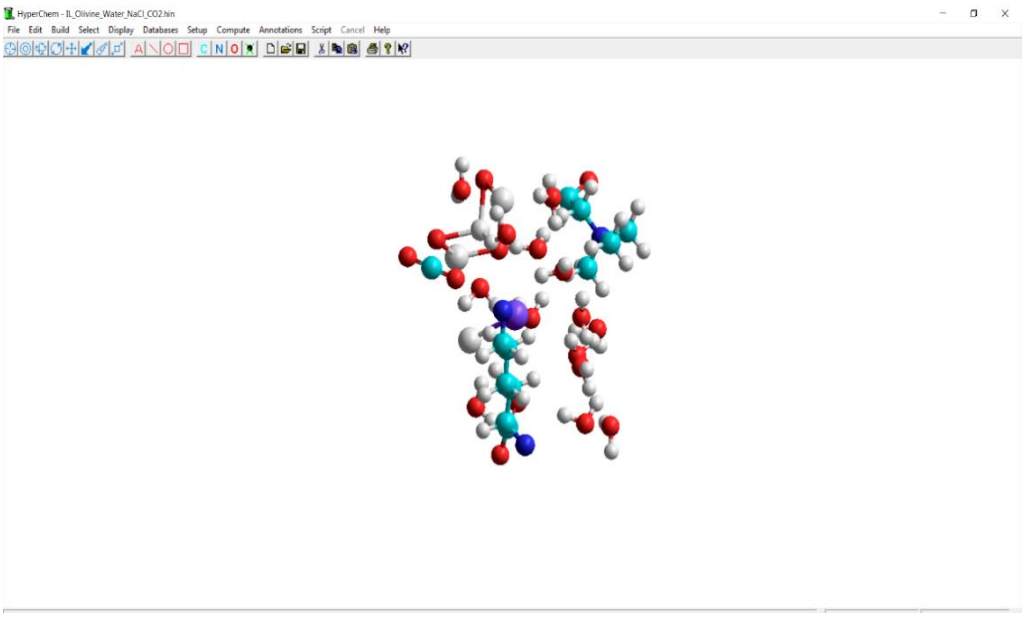

***Figure 23**: HyperChem software interface and workflow.*

After simulation, for the control test, the result of Ea is 25.2 kcal/mol which is a realistic activation energy. This value can be due to mild hydrolysis, dissolution, or ion coordination. The reactions occurring at or near room temperature and ILs that are used can enhance dissolution of minerals. For the carbonation test, the result for Ea is 11.8 kcal/mol which is physically meaningful. CO_2 involvement may cause reaction steps like mineral carbonation, lysine carbamate formation, and ion exchange on the olivine surface.

Chapter 3

Testing results and discussion

3.1 ATR-IR

Attenuated Total Reflectance Fourier Transform Infrared Spectroscopy (ATR-FTIR) was employed to confirm the structural integrity and interactions of choline-based ionic liquid solutions, including [Cho][Lys] and [Cho][Pro]. The spectra provided key insights into the molecular fingerprints and chemical environments of the samples. The infrared (IR) spectra analyzed in this study are presented with the Y-axis in arbitrary absorbance units, while the X-axis shows wavenumbers in cm^{-1}. To enhance the visibility of critical spectral features, the OPUS software was employed to reverse and scale the data, eliminating unreliable signals from the higher wavenumber region (left side), which often suffers from surface reflections. The aforementioned adjustment then allows for much clearer visualization of meaningful absorption peaks from the spectra. The shifts in the positions and intensities of the peaks in the various spectra provided information about the bond dynamics in their respective samples, especially with respect to molecular and ionic interactions.

For [Cho][Lys], the characteristic carboxylate group ($-COO^-$) on a lysinate anion shows an asymmetric stretching that gives rise to an absorption band at about ~1600 cm^{-1} and a symmetric stretch, on the other hand, an absorption around ~1400–1450 cm^{-1}. The solvent spectrum also displayed typical features, including O–H stretches around ~3300–3400 cm^{-1}, C–H stretches near 2900 cm^{-1}, and strong C–O stretching near 1000 cm^{-1}.

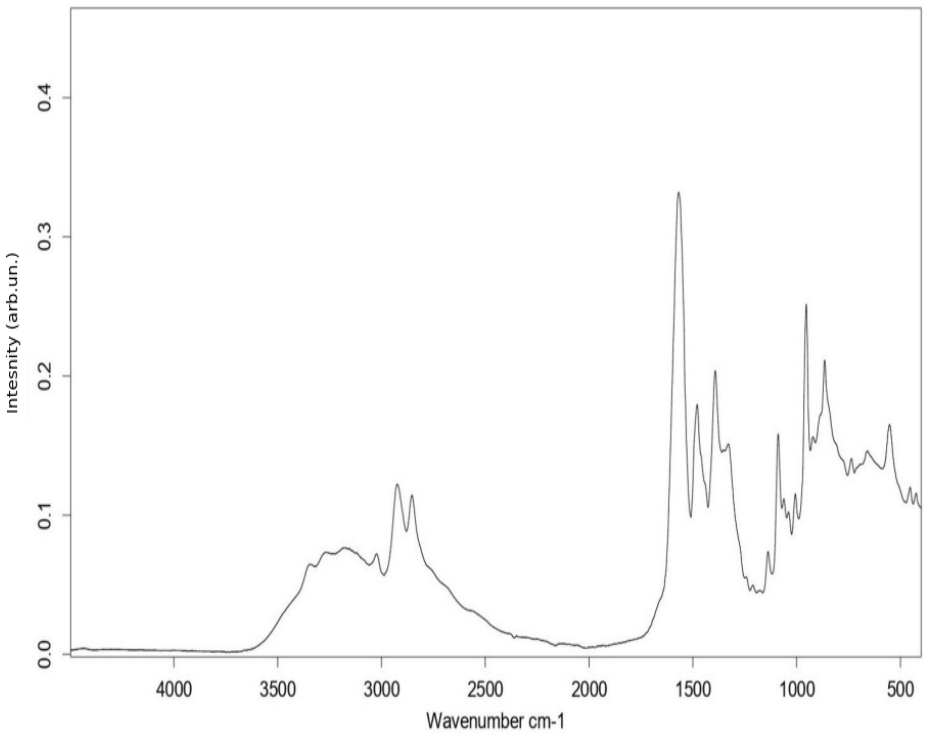

Figure 24: *ATR-IR spectrum of [Cho][Lys].*

The IR spectrum for pure [Cho][Pro] shows fingerprint characterization by several specific bands (see Figure 25) and is related to its molecular structure, primarily associated with the carboxylate (-COO^-) and amine (-NH) groups of the prolinate anion and the hydroxyl (-OH) group of the choline cation.

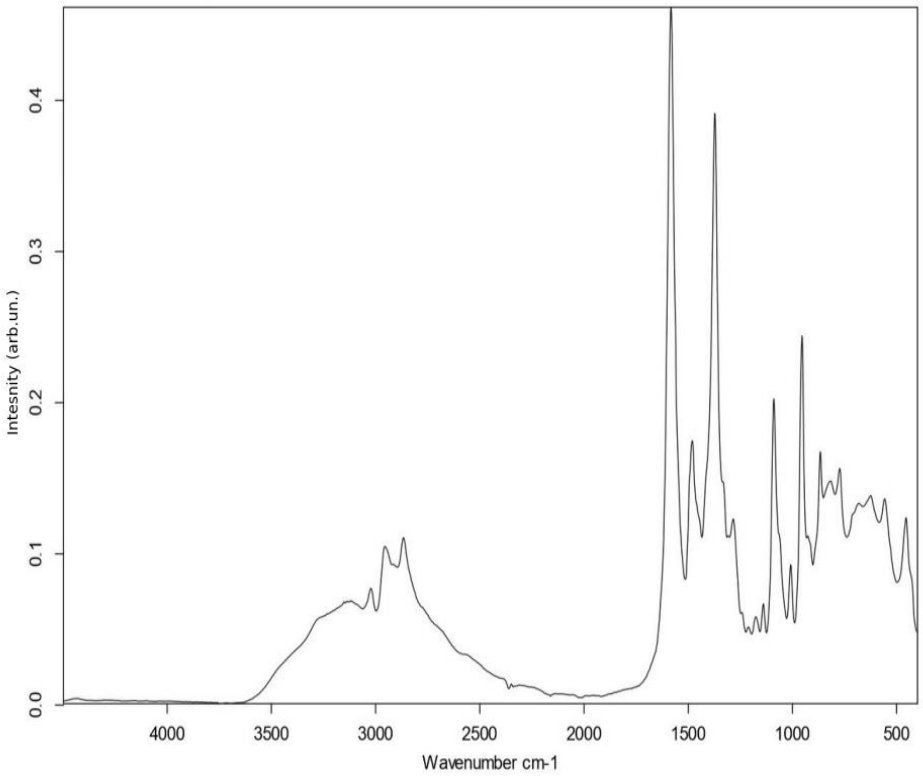

Figure 25: *ATR-IR spectrum of [Cho][Pro].*

A carboxylate group (-COO^-) on a prolinate anion shows an asymmetric stretching that gives rise to an absorption band at about ~1570–1610 cm^{-1} and a symmetric stretch, on the other hand, an absorption around ~1390–1420 cm^{-1}. Moreover, there is a broad absorption with wavenumbers between ~3100 and 3400 cm^{-1} that corresponds to the stretching vibrations of hydrogen-bonded O–H and N–H, emphasizing strong intermolecular hydrogen bonding, which is typical for choline-based ionic liquids. C–N stretching vibrations within the range of 1000–1100 cm^{-1} assigned to the choline cation allow an additional affirmation of the identity of this compound's structure. These peaks suggest the spectral fingerprint of pure [Cho][Pro], before it interacts with CO_2 or undergoes dilution in a solvent. The broad OH/NH stretching band in the ~3100–3400 cm^{-1} region depicts strong intermolecular hydrogen bonding, a common feature in choline-based ILs.

Table 6: *ATR-IR Peak Assignment: [Cho][Lys] vs [Cho][Pro].*

Wavenumber (cm^{-1})	[Cho][Lys] Observation	[Cho][Pro] Observation	Interpretation
~3300–3400	Broad, strong band (O–H/ N–H stretch)	Broad, slightly less intense	[Cho][Lys] has more H-bond donors (NH_2 groups), leading to stronger and broader peaks
~2900–3000	Sharp doublet (C–H stretch)	Similar sharp peaks	Common alkyl C–H stretching in choline present in both
~1600–1650	Moderate–strong peak	Much sharper, stronger peak	[Cho][Pro] shows prominent COO^- asymmetric stretch; more distinct due to less hydrogen bonding overlap
~1400–1450	Moderate intensity	Slightly sharper	COO^- symmetric stretch / CH_2 scissoring — typical in both
~1250–1350	Less diagnostic, but present	Similar trend	CH bending / wagging
~1000–1200	Complex region, multiple bands	More resolved, sharper peaks	C–N stretch, C–O vibrations, fingerprint region — more resolved in [Cho][Pro]
~600–950	Broad, noisy fingerprint peaks	Similar but a few sharper features	Structural differences (e.g., cyclic proline ring) reflected here

As a comparison, it is obvious that hydrogen bonding is stronger/more complex in [Cho][Lys], due to two amine groups on lysine. This leads to broader and slightly shifted N–H/O–H peak bands in the 1600–3300 cm^{-1} region. On the other hand, [Cho][Pro] has sharper COO^- and C–N peaks, probably because proline's secondary amine and ring structure result in fewer overlapping interactions. Also, the 1600 cm^{-1} peak is noticeably more intense and defined in [Cho][Pro], suggesting a more isolated carboxylate stretch, typical for proline-based systems.

3.2 TGA

Figure 26 is a TGA curve representative of the [Cho][Pro]. Impurities may be the reason for the first degradation, as the graph shows. The mass change indicates a very short percentage of loss. Its onset temperature is about 175.6 °C. The thermogravimetric analysis (TGA) of the choline–proline ionic liquid clears that the material is thermally stable up to around 185 °C, which marks the onset of decomposition. As indicated by the peak in the derivative thermogravimetric (DTG) curve, the main degradation event occurs between 185 °C and 276 °C, with the most rapid mass loss observed at 256 °C. During this phase, the ionic liquid undergoes

significant thermal decomposition, resulting in a mass loss of approximately 95.6%, which suggests that most of the organic components volatilize or decompose. Beyond this, the material continues to lose mass slightly, with a residual mass of 0.26% remaining at 799.2 °C. These results depict that the choline–proline ionic liquid is suitable for applications requiring moderate thermal stability, and it should be limited to environments below 180 °C to prevent degradation.

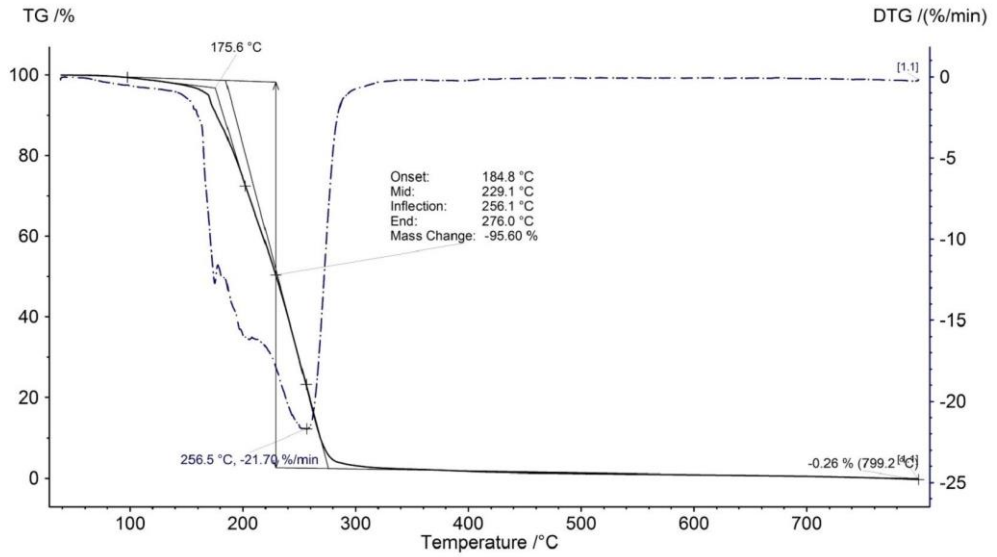

Figure 26: *TGA and its 1st derivative curve for [Cho][Pro].*

Following the TGA analysis of [Cho][Pro], the thermal behavior of [Cho][Lys] is presented in Figure 27. The TGA curve illustrates an initial degradation event beginning at approximately 186 °C, which is slightly higher than the onset temperature of [Cho][Pro]. This initial degradation can be attributed to the loss of low-molecular-weight components or impurities. The inflection point occurs at 193 °C, where the most significant mass loss rate is seen, as indicated by the DTG peak. The main degradation event completed around 193 °C, resulting in a total mass change of approximately 7.82%.

Unlike [Cho][Pro], the [Cho][Lys] ionic liquid exhibits a relatively minor mass loss, suggesting a more stable thermal profile under the specified conditions. A second degradation event is observed at 260.0 °C, but the mass change is relatively small, indicating the decomposition of a more thermally stable component or the evaporation of residual volatiles. Beyond this point, the material maintains stability up to 799.2 °C, with a final residual mass of 1.37%.

These findings indicate that [Cho][Lys] is more thermally stable than [Cho][Pro] in terms of onset decomposition temperature and total mass loss percentage. However, the slight increase in residual mass may suggest incomplete volatilization of certain components or the formation of stable decomposition products. So, for applications requiring higher thermal stability, [Cho][Lys] may be more beneficial than others, and care should be taken to avoid exposure to temperatures above 185 °C to minimize degradation.

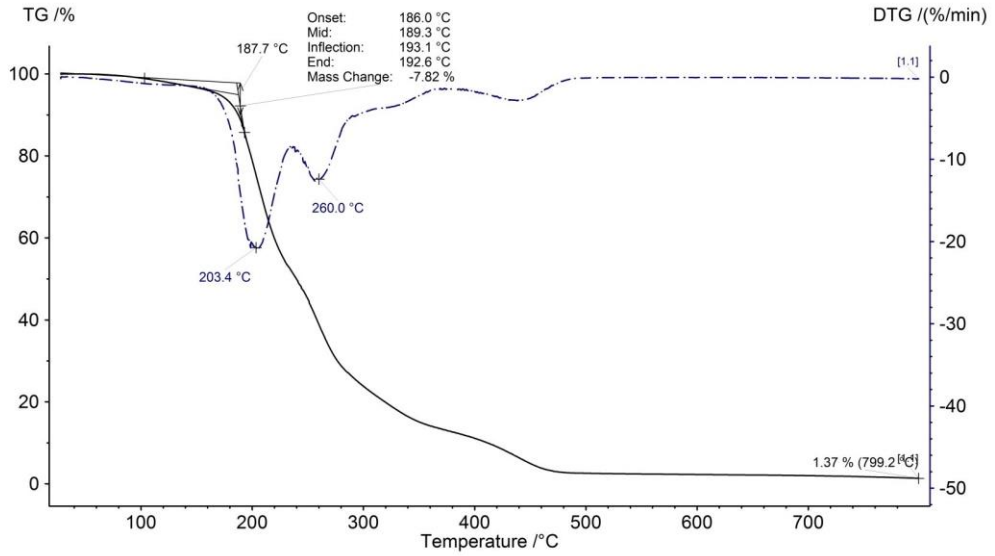

Figure 27: *TGA and its 1st and 2nd derivative curve for [Cho][Lys].*

3.3 X-ray diffraction (XRD)

For this experiment of X-ray diffraction (XRD), precipitation from test related to carbonation condition 1, involving continuous CO_2 bubbling for 30 minutes at room temperature and ambient pressure was used. The powerful matching between the strongest peaks in the XRD sample and those of magnesium carbonate hydrate maintains that carbonation proceeded well. On the other hand, it has become the dominant crystalline product. In addition, the presence of sodium hydrogen carbonate hydrate is likely attributable to excess Na^+ ions introduced via NaCl, which reacted under CO_2-rich aqueous conditions to form this secondary phase. The detection of magnesium oxide carbonate implies the occurrence of incomplete or intermediate carbonation reactions, potentially representing a transient phase in the transformation of olivine. Furthermore, the identification of magnesium iron carbonate hydroxide hydrate implies partial Fe^{2+} release from olivine, reflecting a more

chemically complex environment and possible redox interactions during the reaction process. The subsequent section details the characteristic peak lists for the four most probable reaction products.

Magnesium Carbonate Hydrate with the empirical formula of $C_4H_{10}Mg_5O_{18}$, are frequently created during carbonation of magnesium-rich minerals, such as olivine. They consist of structural water and can exist in various hydrated forms depending on environmental conditions (e.g., temperature, CO_2 pressure). This compound is often formed when CO_2 reacts with aqueous magnesium species, especially in alkaline or mildly basic environments. In XRD, its characteristic peaks near 15.3°, 30.9°, 33.1°, 41.6°, and 53.2° make it easy to identify. Its intense diffraction lines in the sample suggest it may be a major reaction product, supporting the successful carbonation process.

Table 7: *Peak list of Magnesium Carbonate Hydrate.*

No.	h	k	l	d (Å)	2Theta(deg)	I (%)
1				5.80	15.26	100.0
2				2.89	30.91	100.0
3				2.70	33.15	33.0
4				2.48	36.19	33.0
5				2.17	41.58	100.0
6				2.00	45.30	100.0
7				1.72	53.21	66.0
8				1.55	59.59	33.0
9				1.39	67.30	33.0

Magnesium Iron Carbonate Hydroxide Hydrate ($CFe_2H_{28}Mg_{10}O_{29}$) is a more complicated phase involving both magnesium and iron, often observed when ferrous components (e.g., from olivine) are present in solution. The hydroxide and hydrate components indicate precipitation from aqueous solutions under CO_2 influence. Usually, this compound grows under lower pH or a little decreasing circumstances and may exist with pure magnesium carbonate phases. Its existence is suggested by fewer peaks around 20.8°, and 38.4°, indicating it may be a minor or secondary phase.

Table 8: *Peak list of Magnesium Iron Carbonate Hydroxide Hydrate.*

No.	H	k	l	d (Å)	2Theta(deg)	I (%)
1				13.20	6.69	10.0
2				7.83	11.29	5.0
3				6.05	14.63	30.0
4				4.75	18.66	10.0
5				4.62	19.19	5.0
6				4.26	20.83	100.0
7				2.68	33.40	5.0
8				2.34	38.43	20.0
9				1.76	51.91	5.0
10				1.56	59.13	5.0

Magnesium Oxide Carbonate ($C_2Mg_3O_7$) usually appears during the middle stages of carbonation, when not all CO_2 has fully reacted to create pure carbonates. It may indicate a metastable phase or partial carbonation product, especially at early reaction times or low CO_2 availability. Its XRD features include peaks near 14.6°, 25.4°, 29.6°, and 45.3°, which are moderately visible in the sample spectrum. This suggests it could be a transitional phase formed during the carbonation process.

Table 9: *Peak list of Magnesium Oxide Carbonate.*

No.	H	k	l	d (Å)	2Theta(deg)	I (%)
1	1	1	0	6.05	14.63	100.0
2	2	1	1	3.50	25.42	85.0
3	2	2	0	3.01	29.65	25.0
4	3	2	1	2.26	39.85	35.0
5	4	0	0	2.12	42.61	70.0
6	3	3	0	2.00	45.30	20.0
7	4	2	0	1.90	47.83	16.0
8	3	3	2	1.81	50.37	14.0

Sodium Hydrogen Carbonate Hydrate ($C_2H_5Na_3O_8$) may form due to the presence of NaCl in the reaction mixture, especially when water and CO_2 interact with sodium ions. It represents a soluble phase that may precipitate upon evaporation or concentration of solution. Its XRD pattern shows a dense set of medium-to-weak peaks over a wide 2θ range, with strong peaks near 29.1° and 33.9°, some of which overlap with magnesium carbonates. This shows it may be a secondary product, possibly from residual salt or reaction by-products.

Table 10: *Peak list of Sodium Hydrogen Carbonate Hydrate.*

No.	H	K	l	d (Å)	2Theta(deg)	I (%)
1	2	0	0	9.79	9.02	32.6
2	0	0	2	4.94	17.91	5.2
3	4	0	0	4.89	18.09	21.1
4	-4	0	2	4.10	21.63	1.2
5	2	0	2	3.96	22.27	6.6
6	1	1	0	3.43	25.91	2.4
7	6	0	0	3.26	27.29	2
8	1	1	1	3.19	27.88	30.3
9	-6	0	2	3.16	28.18	2.6
10	3	1	0	3.07	29.00	52.6
11	-3	1	1	3.05	29.19	39.3
12	-1	1	2	2.88	30.92	0.6
13	3	1	1	2.83	31.53	0.6
14	-3	1	2	2.78	32.12	5.4
15	1	1	2	2.75	32.42	14.9
16	-5	1	1	2.64	33.86	100
17	5	1	0	2.60	34.36	1.9
18	-2	0	4	2.57	34.79	6.3
19	-4	0	4	2.50	35.79	10.7
20	-8	0	2	2.48	36.04	2
21	0	0	4	2.47	36.32	3.7
22	-1	1	3	2.44	36.80	36.6
23	-3	1	3	2.41	37.19	9
24	1	1	3	2.32	38.73	0.1
25	-6	0	4	2.30	38.99	0.1
26	2	0	4	2.25	39.98	24.3
27	7	1	0	2.18	41.35	1.8
28	5	1	2	2.14	42.06	3.6
29	3	1	3	2.11	42.71	2.5
30	-3	1	4	2.06	43.77	0.8
31	-8	0	4	2.05	44.09	4
32	7	1	1	2.03	44.42	16.9
33	-10	0	2	2.02	44.68	17.2
34	4	0	4	1.99	45.44	4.9
35	-5	1	4	1.98	45.56	4.9
36	8	0	2	1.98	45.68	1.7
37	1	1	4	1.96	46.22	7.9
38	10	0	0	1.95	46.31	5.5
39	-9	1	1	1.89	47.86	1.2
40	-9	1	2	1.88	48.28	5.4

41	-7	1	4	1.85	49.20	1.6
42	9	1	0	1.84	49.30	2.1
43	-9	1	3	1.80	50.52	0.8
44	-10	0	4	1.80	50.63	1.4
45	-3	1	5	1.77	51.44	12.8
46	0	2	0	1.74	52.39	9.2
47	9	1	1	1.74	52.48	14.8
48	0	2	1	1.71	53.28	1.6
49	-4	0	6	1.71	53.36	2.7
50	-2	2	1	1.70	53.65	1.2
51	-12	0	2	1.69	53.93	0.2
52	-9	1	4	1.68	54.41	1.4
53	1	1	5	1.67	54.62	4.7
54	-6	0	6	1.67	54.82	2.8
55	10	0	2	1.66	55.00	1.9
56	7	1	3	1.66	55.26	12.2
57	-7	1	5	1.65	55.36	7.5
58	-4	2	1	1.64	55.77	4.9
59	12	0	0	1.63	56.31	1.6
60	9	1	2	1.60	57.19	0.2
61	-4	2	2	1.60	57.32	0.3
62	2	2	2	1.59	57.66	6.1
63	-11	1	3	1.59	57.81	3.8
64	-8	0	6	1.59	57.94	6.4
65	11	1	0	1.58	58.10	3.5
66	-12	0	4	1.58	58.28	2
67	3	1	5	1.57	58.63	1.1
68	2	0	6	1.55	59.37	1.7
69	-6	2	1	1.55	59.50	1.7
70	0	2	3	1.54	59.97	0.4
71	6	2	0	1.53	60.11	0.4
72	-5	1	6	1.52	60.52	0.5
73	4	2	2	1.51	60.99	3.6
74	6	2	1	1.49	62.21	1.3
75	7	1	4	1.48	62.57	0.1
76	-7	1	6	1.48	62.67	0.2
77	-6	2	3	1.47	63.14	0.4
78	9	1	3	1.46	63.24	0.3
79	1	1	6	1.45	63.73	0.2
80	5	1	5	1.45	64.12	0.3
81	4	0	6	1.44	64.42	0.4
82	-8	2	1	1.44	64.67	0.5
83	12	0	2	1.43	64.92	0.7

84	-4	2	4	1.43	65.04	0.4
85	-8	2	2	1.42	65.23	0.7
86	0	2	4	1.42	65.39	0.4
87	-13	1	1	1.42	65.63	1.3
88	4	2	3	1.41	65.84	0.8
89	-13	1	3	1.41	66.11	2.9
90	-9	1	6	1.40	66.33	1.6
91	14	0	0	1.39	66.80	3
92	-6	2	4	1.39	67.20	0.3
93	-8	2	3	1.38	67.30	0.2
94	3	1	6	1.37	67.88	2
95	8	2	1	1.37	68.11	1.3
96	-12	0	6	1.36	68.54	1
97	10	0	4	1.36	68.93	0.2
98	-3	1	7	1.35	69.32	1.6
99	-5	1	7	1.35	69.40	1.6
100	-2	2	5	1.32	70.81	3.9
101	-4	2	5	1.32	70.94	2.3
102	-10	2	2	1.32	71.26	1.4
103	-11	1	6	1.31	71.40	0.7
104	4	2	4	1.31	71.82	0.4
105	8	2	2	1.31	72.00	0.4
106	11	1	3	1.30	72.18	0.2
107	10	2	0	1.30	72.52	0.9
108	5	1	6	1.28	73.44	0.1
109	1	1	7	1.28	73.64	0.4
110	-6	0	8	1.28	73.85	0.4
111	-9	1	7	1.27	74.05	0.1
112	-16	0	2	1.27	74.34	0.3
113	-2	0	8	1.27	74.51	0.2
114	-15	1	2	1.26	74.89	1.1
115	-15	1	3	1.25	75.38	0.5
116	14	0	2	1.25	75.57	0.5
117	-8	0	8	1.25	75.74	1
118	13	1	2	1.25	75.98	0.5
119	-16	0	4	1.24	76.44	0.8
120	0	0	8	1.23	77.03	0.1
121	6	2	4	1.23	77.14	0.1
122	-15	1	4	1.23	77.34	0.1
123	3	1	7	1.22	77.97	0.3
124	-2	2	6	1.22	78.29	0.2
125	-11	1	7	1.21	78.51	0.3
126	9	1	5	1.21	78.80	0.6

127	-10	0	8	1.20	79.10	1
128	-5	1	8	1.20	79.21	0.6
129	10	2	2	1.20	79.43	0.7
130	-12	2	3	1.20	79.63	0.4
131	0	2	6	1.19	79.98	0.4
132	7	1	6	1.19	80.21	0.3
133	-7	1	8	1.19	80.33	0.2
134	12	2	0	1.19	80.50	0.6
135	-15	1	5	1.18	80.70	0.3
136	2	0	8	1.18	80.96	0.6
137	15	1	1	1.17	81.77	0.3
138	-8	2	6	1.17	81.89	0.6
139	13	1	3	1.17	82.18	1.4
140	-9	1	8	1.16	82.86	0.1
141	2	2	6	1.16	83.08	0.2
142	12	2	1	1.15	83.59	0.1
143	-12	0	8	1.15	83.77	0.2
144	-16	0	6	1.14	84.14	0.5
145	-13	1	7	1.14	84.32	0.4
146	1	1	8	1.14	84.47	0.4
147	-3	3	1	1.14	84.63	0.3
148	6	2	5	1.14	84.67	0.2
149	10	2	3	1.14	84.90	0.1
150	-17	1	2	1.13	85.57	0.1
151	-17	1	3	1.13	85.69	0.2
152	-18	0	2	1.13	85.79	0.2
153	-12	2	5	1.12	86.09	1.7

The goal of this XRD analysis is to identify the crystalline phases formed after reacting choline lysine, water, NaCl, olivine, and CO_2. The reaction is expected to result in the carbonation of magnesium-rich minerals and possible interaction with sodium-based species.

Table 11: *X-Ray Diffraction Analysis of Sample Compounds.*

Feature	Observation in Sample	Related Compound
Sharp, intense peak at ~31°	Strongest peak	Magnesium Carbonate Hydrate
Multiple peaks around 40°–50°	Moderate and sharp	Magnesium Carbonate Hydrate, Magnesium Oxide Carbonate
Peak at ~20°	Very weak	Magnesium Iron Carbonate Hydroxide Hydrate
Moderate peak at ~29°	Moderate in sample	Sodium Hydrogen Carbonate Hydrate
Broad distribution of small peaks	Seen from 20° to 60°	Sodium Hydrogen Carbonate Hydrate (numerous weak peaks)

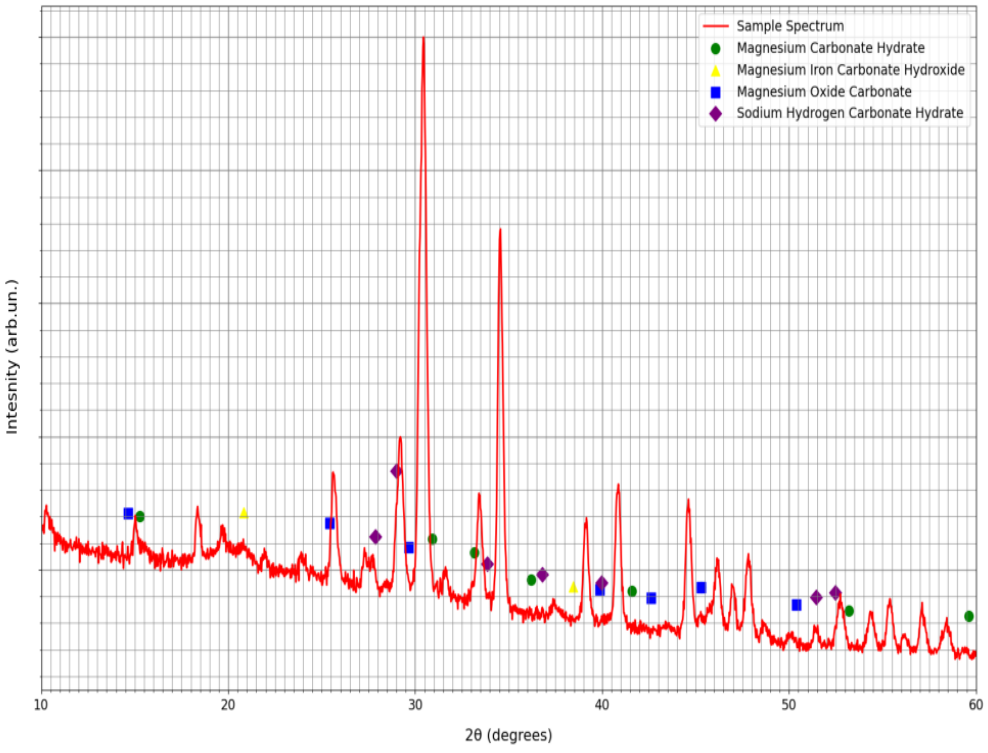

Figure 28: *X-Ray Diffraction pattern with reference peaks.*

3.4 Raman Spectroscopy

Three Raman spectra illustrations (Figures 29, 30, and 31) were selected for detailed analysis based on their arbitrary unit intensity ranges and spectral quality, providing insight into the molecular-level changes taking place during the reaction process and the probability of successful CO_2 incorporation.

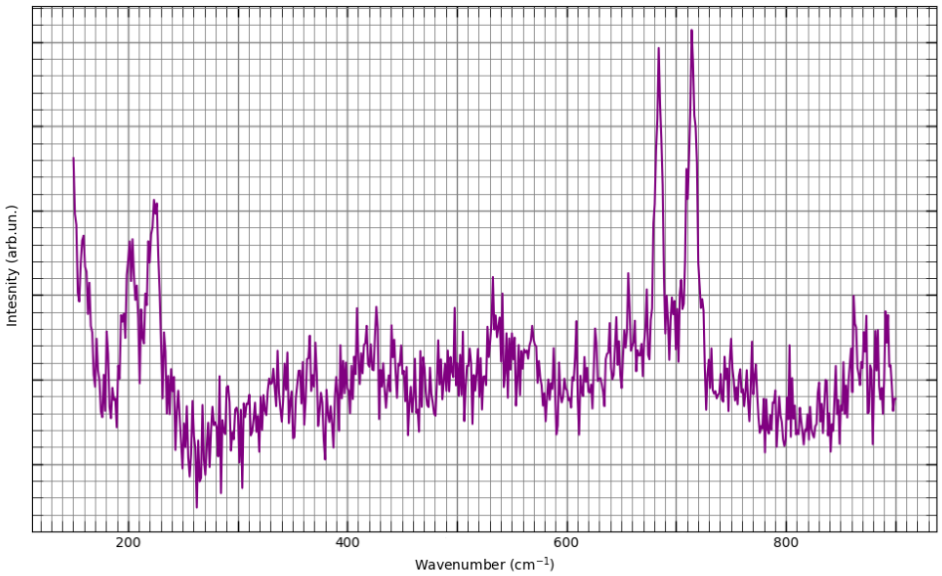

Figure 29: *Raman spectrum 1.*

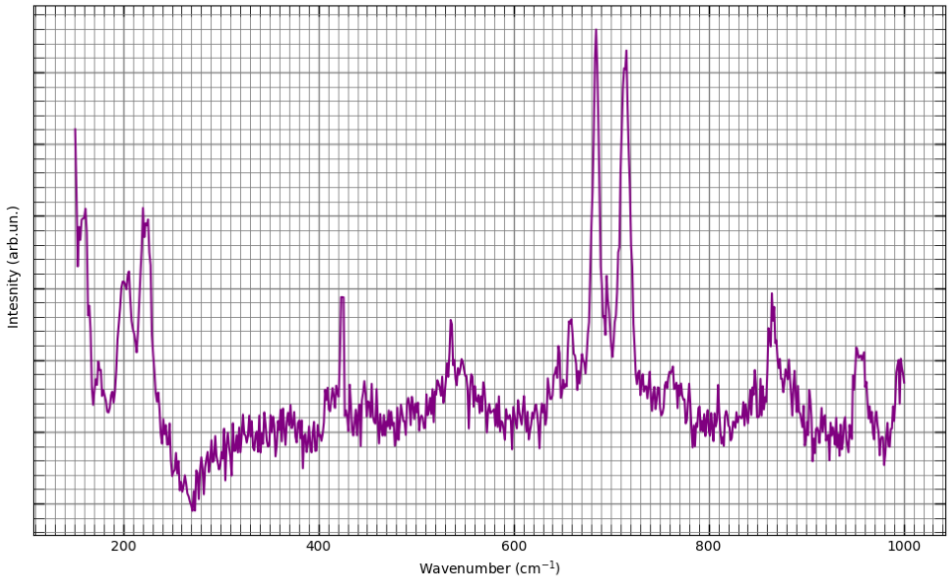

Figure 30: *Raman spectrum 2.*

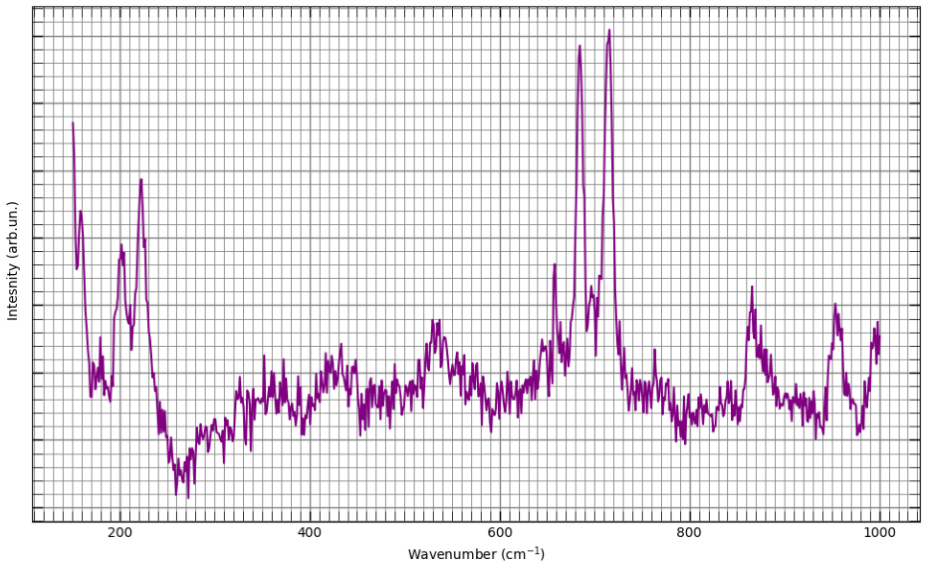

Figure 31: *Raman spectrum 3.*

The spectral analysis indicates significant confirmation for chemical transformation and potential CO_2 capture systems within the reaction. The most striking feature across all three spectra is the emergence of prominent peaks in the 650-700 cm^{-1} region, which represents a substantial deviation from pure olivine signatures and indicates the formation of new chemical phases. These peaks are consistently noticed across all measurements, with spectrum 29 showing peaks at approximately 680 and 720 cm^{-1}, spectrum 30 demonstrating similar features around 650-680 cm^{-1}, and spectrum 31 exhibiting comparable spectral activity in this critical region. This spectral region is particularly significant as it may align with carbonate stretching modes, altered silicate structures resulting from CO_2 interaction, or reaction products between the ionic liquid and mineral phases under CO_2-rich conditions. Also, the spectra list additional complexity in the 800-900 cm^{-1} region, where new peaks suggest the formation of secondary reaction products or phase changes that could be considered as CO_2 capture and subsequent chemical stabilization.

The comparison between the three spectra shows incredible consistency in peak positions and relative intensities, indicating that the observed chemical changes are reproducible and represent genuine reaction products rather than measurement artifacts. All three spectra ensure similar baseline characteristics with excellent signal-to-noise ratios, suggesting stable reaction conditions and uniform product formation across different sampling locations. The spectral features in the low-frequency region (150-300 cm^{-1}) show some variation between samples.

The intensity variation across spectra indicates different measurement conditions.
Several factors of the assessment of CO_2 capture probability based on this comprehensive Raman spectroscopic evidence indicate a high likelihood of successful CO_2 incorporation into the system. The consistent image of spectral features in the 650-700 cm^{-1} region across all three measurements provides compelling evidence for carbonate formation or CO_2-related chemical modifications. They may represent carbonate species in modified chemical environments, such as surface-bound carbonates on olivine, carbonate-silicate interaction products, or CO_2 species coordinated within the ionic liquid matrix.
The presence of choline lysine in the system offers multiple pathways for CO_2 capture, including direct absorption into the ionic liquid phase followed by transfer to the mineral surface or facilitation of mineral carbonation through pH modification and enhanced CO_2 solubility. The spectral complexity noted, particularly the multiple peak features in different regions, states that CO_2 incorporation occurs through several simultaneous mechanisms, potentially including both ionic liquid absorption and mineral carbonation pathways.

3.5 Tecno Delta thermostatized room

In this series of experiments, for carbonation condition test 3, the experiment is based on a 25 mL solution total volume. With the molar mass of cholinium-lysinate (249.35 g/mol), 12.5 grams of IL correspond to approximately 0.05013 mol of cholinium. An equal mass of water (12.5 grams) completes the 50 wt% solution. To match the molar concentration of cholinium, 2.92 grams of NaCl are added, calculated from its molar mass (58.44 g/mol). Olivine is added such that the amount of magnesium available for dissolution corresponds to 0.02506 mol, i.e., half the amount of cholinium, resulting in approximately 1.76 grams of olivine per test (see Table 12).

Table 12: *Summary table for carbonation condition 3 experiment with ILs.*

[Cho][Lys] 50%	equivalents	MW (g/mol)	m (g)	Mol
[Cho][Lys]	1	249.35	12.5	0.05
Water	14	18	12.5	0.69
NaCl	1	58.44	2.92	0.05
Mg_2SiO_4	0.5	140.69	1.76	0.025

The blank experiment was performed by using just water, without using ILs. For this carbonation condition test 3, the experiment is based on a 25 mL solution total volume. With the molar mass of water (18 g/mol), 25

grams of water correspond to approximately 1.38 mol of it. To match the molar concentration of water, 5.85 grams of NaCl are added, calculated from its molar mass (58.44 g/mol). Olivine is added that the amount of magnesium available for dissolution corresponds to 0.05 mol, resulting in approximately 3.52 grams of olivine per test (see Table 13).

Table 13: *Summary table for carbonation condition 3 experiment without ILs.*

[Cho][Lys] 50%	equivalents	MW (g/mol)	m (g)	Mol
[Cho][Lys]	-	-	-	-
Water	14	18	25	1.38
NaCl	1	58.44	5.85	0.10
Mg_2SiO_4	0.5	140.69	3.52	0.05

Following the preparation of the two test solutions, each was subjected to a separate experimental run under identical conditions. In both cases, the 50 mL reactors were filled with 25 mL of solution and placed within the thermostatically controlled chamber. The chamber temperature was maintained at a constant 50 °C, and carbon dioxide was introduced into the system at an initial pressure of 5 bar.
Each test required approximately three days for the system pressure to stabilize. In the first experiment which the test solution consisted of an ionic liquid (IL) and water mixture, the pressure stabilized at 3.5 bar.
In the second experiment, a control solution composed solely of water was used. In this case, the pressure stabilized at 2.5 bar after the same period.
In the experiments, the IL + water system used 1.76 g of olivine and resulted in a 1.5 bar drop in CO_2 pressure, while the water-only system used 3.52 g of olivine and showed a 2.5 bar pressure drop. To compare their performance, the CO_2 uptake per gram of olivine was calculated: 0.852 bar/g for the IL system and 0.710 bar/g for the water system. This shows that the IL + water mixture achieved approximately 20% higher carbonation efficiency per gram of olivine. Despite a smaller total pressure drop, the IL system used the mineral more effectively, suggesting that ionic liquids enhance magnesium extraction and CO_2 utilization, making the process more efficient and resource-conscious.

3.6 Simulation

According to the results, E_a is lower for the case with CO_2 insufflation which shows the energy barrier for the reaction is smaller. According to the Arrhenius equation lower E_a results in a higher rate constant k at a given temperature (see Equation 1). Therefore, adding CO_2 increases the reaction rate (i.e., increases k) in this case.

For determination of the temperature effect, using the Arrhenius Equation is beneficial (see Equation 1). Because by knowing activation energy, it is possible to estimate reaction rates k at different temperatures T (see Figure 32). Therefore, for example at temperature equal to 25 degrees Celsius, adding CO_2 increases the reaction rate by a factor of 10^8, meaning the reaction will be 10^8 times faster, or the reaction time will be 10^8 times shorter.

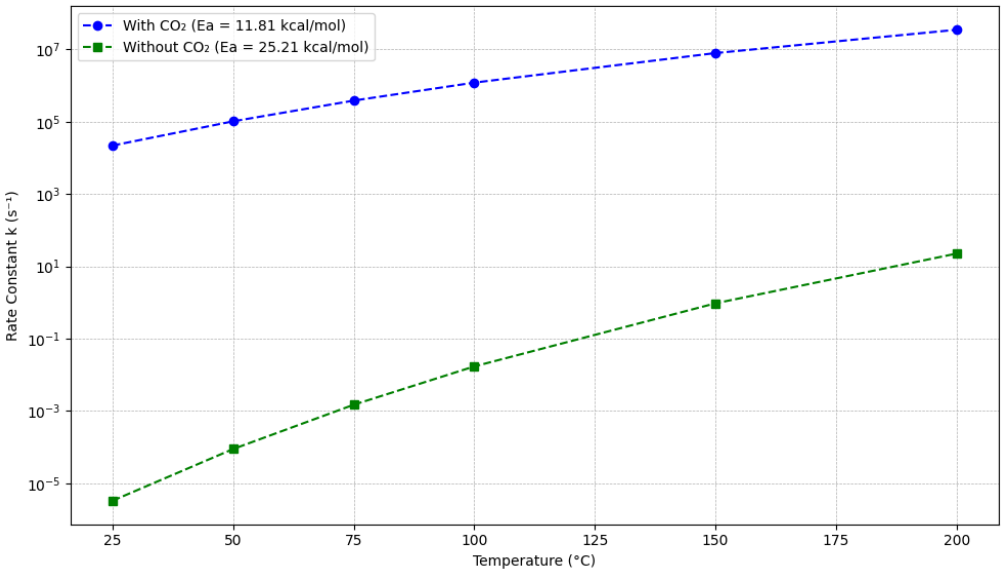

Figure 32: *Arrhenius plot: reaction rate vs temperature with and without CO_2.*

The rate grows exponentially as the temperature rises. At room temperature (25°C), the reaction is extremely slow, but at 100°C and above, the rate becomes much more significant supporting the idea of why heating is often used in IL-mineral systems. At 200°C, which is near industrial conditions, the reaction could occur on a seconds-to-minutes timescale.

Table 14: *Impact of CO_2 on Reaction Kinetics and Practical Application.*

Factor	With CO_2	Without CO_2
Activation Energy	Lower (11.8 kcal/mol)	Higher (25.2 kcal/mol)
Reaction Rate (k)	Higher at all T	Lower
Sensitivity to T	Moderate	Higher
Ease of Control	More complex setup	Simpler setup
Industrial Suitability	Better at low T	High cost due to heating

The Arrhenius analysis shows a significant improvement in kinetics when CO_2 is presented with the system (olivine, water, choline lysinate, and

NaCl). The activation energy decreases significantly from 25.2 kcal/mol in the test without CO_2 to 11.8 kcal/mol in the presence of CO_2. This reduction in activation energy causes much larger reaction rates across all temperatures tested. The temperature-dependent rate constants demonstrate the profound catalytic effect of CO_2, where at 50°C, the rate constant in the CO_2-containing system is several orders of magnitude greater than the system without CO_2. This improvement also gets more evident at lower temperatures, proving that CO_2 enables the reaction to continue well under lower thermal conditions.

The comparative analysis between the two systems reveals stark differences in performance characteristics. With CO_2 present (E_a = 11.8 kcal/mol), the system exhibits enhanced reaction kinetics due to lower activation energy barriers, efficient operation at moderate temperatures including near ambient conditions (~25°C), reduced energy requirements for industrial implementation, and faster reaction rates enabling shorter processing times. However, without CO_2 (E_a = 25.2 kcal/mol), the system has issues with significantly slower reaction kinetics requiring higher activation energy, substantial temperature increases (>150°C) needed for industrially viable rates, higher energy demands and operational costs, and limited applicability under mild reaction conditions.

The catalytic function of CO_2 probably includes multiple pathways that collectively enhance the reaction efficiency. CO_2 may participate directly in the reaction mechanism by stabilizing intermediate species or activating functional groups, particularly hydroxyl groups on the olivine surface. Additionally, CO_2 can shift chemical equilibria toward protonation or bicarbonate formation, facilitating acid-promoted dissolution of olivine minerals—a process particularly important in geochemical systems. The synergistic relationship between CO_2 and the ionic liquid choline lysinate implies another important factor. Ionic liquids are known to develop favorable interactions with CO_2, potentially creating carbamate species or hydrogen-bond networks that further activate the reaction system and enhance overall performance.

The kinetic improvement provided by CO_2 offers a number of benefits for possible applications. The ability to achieve high reaction rates at lower temperatures reduces operational costs and minimizes equipment stress, making the process more economically viable. Furthermore, the system transforms CO_2 from a waste product into a valuable reaction enhancer, creating opportunities for carbon sequestration while improving process efficiency. Shorter reaction times result from faster kinetics, advantageous to both laboratory-scale research and industrial-scale applications. It is useful for the dissolving of minerals, metal recovery, and CO_2 capture using silicate rocks. The simulation results confirm that CO_2 acts as a powerful facilitator in this complex reaction environment, making the system more reactive and industrially feasible at lower temperatures. This improved

performance complies with current goals in sustainable mineral processing, carbon capture technologies, and green chemistry initiatives, where operational efficiency under mild conditions is paramount. The dramatic reduction in activation energy demonstrates that CO_2 addition transforms the reaction from a high-temperature, energy-intensive process to one that can operate efficiently under moderate thermal conditions, significantly expanding its potential for practical implementation.

Chapter 4

Conclusion, and Future work

4.1 Conclusion

This thesis pursued the application of choline-based amino acid ionic liquids ([Cho][Pro] and [Cho][Lys]) for CO_2 capture and olivine dissolution, dealing with the urgent need for sustainable carbon sequestration technologies. Key findings include:

1. **Synthesis and Characterization:** The ILs were successfully synthesized and exhibited excellent thermal stability (> 175°) and structural integrity, as confirmed by ATR-IR and TGA-IR. Their biocompatibility and low volatility make them ideal for green chemistry applications.
2. **CO_2 Capture and Mineralization:** [Cho][Lys] demonstrated excellent performance in accelerating olivine dissolution and CO_2 mineralization, with XRD demonstrating magnesium carbonate hydrates as most reaction products. Raman spectroscopy further validated CO_2 integration into the system.
3. **Kinetic Improvements**: Computational simulations confirmed that CO_2 significantly declined the activation energy of the dissolution operation (from 25.2 to 11.8 kcal/mol), assisting reactions at moderate temperatures effectively. This catalytic impact emphasizes the potential of CO_2 as a reaction enhancer in industrial CCS processes.
4. **Environmental and Industrial Relevance**: The study highlights the dual benefit of ChoAAILs, simultaneously capturing CO_2 and facilitating mineral carbonation, while operating under mild conditions. This aligns with global efforts to reduce energy-intensive CCS methods.

4.2 Future work

The experiments carried out in this first phase were intended to explore whether ionic liquids could offer a promising route for olivine dissolution and, more broadly, for CO_2 capture through mineral carbonation. While the results are still preliminary, they point to directions worth investigating further. Future work should focus on clearly defining the reaction kinetics and carefully characterizing the materials involved, also keeping in mind the importance of developing a process that is economically scalable and competitive with existing carbon capture technologies.
In conclusion, this work proceeds the development of sustainable solvents for carbon management, offering a feasible, eco-friendly substitute to conventional amine-based systems. The synergy between ionic liquids and mineral carbonation exemplifies an innovative approach to addressing the global CO_2 challenge.

References

[1] Intergovernmental Panel on Climate Change (IPCC). Climate Change 2021: The Physical Science Basis.

[2] Intergovernmental Panel on Climate Change (IPCC). Climate Change 2022: Impacts, Adaptation and Vulnerability.

[3] Oelkers, E. H., Declercq, J., & Saldi, G. D. (2018). Olivine dissolution rates: A critical review. Chemical Geology, 500, 1–19.

[4] Velbel, M.A., 2009. Dissolution of olivine during natural weathering. Geochim. Cosmochim. Acta 73, 6098–6113.

[5] Oelkers, E.H., 2001a. General kinetic description of multioxide silicate mineral and glass dissolution. Geochim. Cosmochim. Acta 65, 3703–3719.

[6] Rimstidt, J.D., Brantley, S.L., Olsen, A.A., 2012. Systematic review of forsterite dissolution rate data. Geochim. Cosmochim. Acta 99, 159–178.

[7] Crundwell, R.K., 2014. The mechanism of dissolution of forsterite, olivine and minerals of the orthosilicate group. Hydrometallurgy 150, 68–82.

[8] Brown, G.E., 1980. Olivines and silicate spinels. Rev. Mineral. Geochem. 5, 275–381. Brunauer, S., Emmett, P.H., Teller, F., 1938. Adsorption of gases in multimolecular layers. J. Am. Chem. Soc. 60, 309–319.

[9] Putnis, A., 1992. Introduction to Mineral Sciences. Cambridge University Press (457 pp.).

[10] Oelkers, E.H., Schott, J., 2001. An experimental study of enstatite dissolution rates as a function of pH, temperature, and aqueous Mg and Si concentration, and the mechanism of pyroxene/pyroxenoid dissolution. Geochim. Cosmochim. Acta 65, 1219‐1231.

[11] Saldi, G.D., Kohler, S.J., Marty, N., Oelkers, E.H., 2007. Dissolution rates of talc as a function of solution composition, pH and temperature. Geochim. Cosmochim. Acta 71, 3446‐3457.

[12] Casey, W.H., Sposito, G., 1993. On the temperature dependence of mineral reaction rates. Geochim. Cosmochim. Acta 56, 3825‐3830.

[13] Brunauer, S., Emmett, P.H., Teller, F., 1938. Adsorption of gases in multimolecular layers. J. Am. Chem. Soc. 60, 309‐319.

[14] Brantley, S.L., Mellott, N.P., 2000. Surface area and porosity of primary silicate minerals. Am. Mineral. 85, 1767‐1783.

[15] Weber, S., Martinez, R.E., 2017. Effects of *Synechococcus* sp. cyanobacteria inert biomass on olivine dissolution: implications for the application of enhanced weathering methods. Appl. Geochem. 84, 162‐172.

[16] Shirokova, L.S., Benezeth, P., Pokrovsky, O.S., Gerard, E., Menez, B., Alfredsson, H., 2012. Effect of the heterotrophic bacterium *Psuedomonas*

reactans on olivine dissolution kinetics and implications for CO2 storage in basalts. Geochim. Cosmochim. Acta 80, 30‑50.

[17] Schott, J., Pokrovsky, O.S., Oelkers, E.H., 2009. The link between mineral dissolution/precipitation kinetics and solution chemistry. Rev. Mineral. Geochem. 70, 207–258.

[18] Velbel, M.A., 1999. Bond strength and the relative weathering rates of simple orthosilicates. Am. J. Sci. 299, 679–696.

[19] P. Walden, Ueber die molekulargrosse und elektrische leitfahigkeiteiniger gesehmolzenen salze, Bull. Acad. Imper. Sci (St Petersburg) 8 (6) (1914) 405–422.

[20] N.V. Plechkova, K.R. Seddon, Applications of ionic liquids in the chemical industry, Chem. Soc. Rev. 37 (1) (2008) 123–150.

[21] Gadilohar, B.L. and G.S. Shankarling, *Choline based ionic liquids and their applications in organic transformation.* Journal of Molecular Liquids, 2017. 227: p. 234-261.

[22] J.P. Hallett, T. Welton, Room-temperature ionic liquids: solvents for synthesis and catalysis. 2, Chem. Rev. 111 (May (5)) (2011) 3508–3576.

[23] C. Verma, E.E. Ebenso, M.A. Quraishi, Corrosion inhibitors for ferrous and non-ferrous metals and alloys in ionic sodium chloride solutions: a review, J. Mol. Liq. 248 (2017) 927–942.

[24] Kaur, G., H. Kumar, and M. Singla, *Diverse applications of ionic liquids: A comprehensive review.* Journal of Molecular Liquids, 2022. 351: p. 118556.

[25] Rogers, R.D. and K.R. Seddon, *Ionic Liquids--Solvents of the Future?* Science, 2003. 302(5646): p. 792-793.

[26] Oelkers, E.H., Benning, L.G., Lutz, S., Mavromatis, V., Pearce, C.R., Plumper, O., 2015. The efficient long-term inhibition of forsterite dissolution by common soil bacteria and fungi at Earth surface conditions. Geochim. Cosmochim. Acta 168, 222‑235.

[27] Hayes, R., G.G. Warr, and R. Atkin, *Structure and Nanostructure in Ionic Liquids.* Chemical Reviews, 2015. 115(13): p. 6357-6426.

[28] Zhang, X., et al., *Carbon capture with ionic liquids: overview and progress.* Energy & Environmental Science, 2012. 5(5): p. 6668-6681.

[29] Greaves, T.L. and C.J. Drummond, *Protic Ionic Liquids: Properties and Applications.* Chemical Reviews, 2008. 108(1): p. 206-237.

[30] Lee, S.-g., *Functionalized imidazolium salts for task-specific ionic liquids and their applications.* Chemical Communications, 2006(10): p. 1049-1063.

[31] de Jesus, S.S. and R. Maciel Filho, *Are ionic liquids eco-friendly?* Renewable and Sustainable Energy Reviews, 2022. 157: p. 112039.

[32] Płotka-Wasylka, J., et al., *Deep eutectic solvents vs ionic liquids: Similarities and differences.* Microchemical Journal, 2020. 159: p. 105539.

[33] Wasserscheid, P. and W. Keim, *Ionic Liquids—New "Solutions" for Transition Metal Catalysis.* Angewandte Chemie International Edition, 2000. 39(21): p. 3772-3789.

[34] Ebrahimi, M., et al. *A Review on Ionic Liquids-Based Membranes for Middle and High Temperature Polymer Electrolyte Membrane Fuel Cells (PEM FCs)*. International Journal of Molecular Sciences, 2021. 22, DOI: 10.3390/ijms22115430.
[35] Ratti, R., *Ionic Liquids: Synthesis and Applications in Catalysis.* Advances in Chemistry, 2014. 2014(1): p. 729842.
[36] Bhattacharyya, S., Shah, F. U., & Mikkola, J.-P. (2016). Ether functionalized choline tethered amino acid ionic liquids for enhanced CO_2 capture. *ACS Sustainable Chemistry & Engineering*, 4(10), 5441–5449.
[37] Zeisel, S.H. and K.A. da Costa, *Choline: an essential nutrient for public health.* Nutr Rev, 2009. 67(11): p. 615-23.
[38] Daintith, J., *The Facts on File Dictionary of Organic Chemistry*. 2014: Facts On File, Incorporated.
[39] M. Petkovic, et al., Novel biocompatible cholinium-based ionic liquids toxicity and biodegradability, Green Chem. 12 (4) (2010) 643–664.
[40] W. Gouveia, et al., Toxicity of ionic liquids prepared from biomaterials, Chemosphere 104 (2014).
[41] R.E. Kirk, et al., Kirk-Othmer Encyclopedia of Chemical Technology, 4th ed., John Wiley & Sons, Inc, 2000.
[42] T.M. Lammens, M.C.R. Franssen, E.L. Scott, J.P.M. Sanders, Availability of protein-derived amino acids as feedstock for the production of bio-based chemicals, Biomass Bioenergy 44 (September) (2012) 168–181.
[43] Tao, G.-h., et al., *Preparation, characterization and application of amino acid-based green ionic liquids.* Green Chemistry, 2006. 8(7): p. 639-646.
[44] Bara, J. E., *Absorption-Based Post-combustion Capture of Carbon Dioxide*. 2016; p Pages 259-282.
[45] Kirchhecker, S.; Esposito, D., Amino acid based ionic liquids: A green and sustainable perspective. *Current Opinion in Green and Sustainable Chemistry* 2016, *2*, 28-33.
[46] Mumford, K. A.; Wu, Y.; Smith, K. H.; Stevens, G. W., Review of solvent based carbon-dioxide capture technologies. *Frontiers of Chemical Science and Engineering* 2015, *9* (2), 125-141.
[47] Aghel, B.; Janati, S.; Wongwises, S.; Shadloo, M. S., Review on CO2 capture by blended amine solutions. *International Journal of Greenhouse Gas Control* 2022, *119*.
[48] Li, W., et al., *Mechanism and Kinetic Study of Carbon Dioxide Absorption into a Methyldiethanolamine/1-Hydroxyethyl-3-methylimidazolium Lysine/Water System.* Energy & Fuels, 2018. 32(10): p. 10813-10821.
[49] S. Zeng, et al., Ionic-liquid-based CO2 capture systems: structure, interaction and process, Chem. Rev. 117 (14) (2017) 9625–9673.
[50] G. Cui, J. Wang, S. Zhang, Active chemisorption sites in functionalized ionic liquids for carbon capture, Chem. Soc. Rev. 45 (15) (2016) 4307–4339.
[51] Yang, Q.; Sheng, M.; Henkelis, J. J.; Tu, S.; Wiensch, E.; Zhang, H.; Zhang, Y.; Tucker, C.; Ejeh, D. E., Explosion Hazards of Sodium Hydride in Dimethyl

Sulfoxide, N,N-Dimethylformamide, and N,N-Dimethylacetamide. *Organic Process Research & Development* 2019, *23* (10), 2210-2217.

[52] Felix, F.; Letti, L. A. J.; Vinicius de Melo Pereira, G.; Bonfim, P. G. B.; Soccol, V. T.; Soccol, C. R., L-lysine production improvement: a review of the state of the art and patent landscape focusing on strain development and fermentation technologies. *Crit Rev Biotechnol* 2019, *39* (8), 1031-1055.

[53] D'Este, M.; Alvarado-Morales, M.; Angelidaki, I., Amino acids production focusing on fermentation technologies - A review. *Biotechnol Adv* 2018, *36* (1), 14-25.

[54] Water - Density, S. W. a. T. E. C. The Engineering ToolBox. ttps://www.engineeringtoolbox.com/water-density-specific-weight-d_595.html.

[55] Gong, Y., X. Chen, and W. Wu, *Application of fourier transform infrared (FTIR) spectroscopy in sample preparation: Material characterization and mechanism investigation.* Advances in Sample Preparation, 2024. 11: p. 100122.

[56] Grandstaff, D.E., 1978. Changes in surface area and morphology and the mechanism of forsterite dissolution. Geochim. Cosmochim. Acta 42, 1899-1901.

[57] Cullity, B. D. (2001). Elements of x-ray diffraction. Stuart R. Stock (3rd ed.). Upper Saddle River, NJ: Prentice Hall. ISBN 0-201-61091-4. OCLC 46437243.

[58] Guinier A (1952). X-ray Crystallographic Technology. London: Hilger and Watts LTD. p. 271.

[59] Barron, A, and A. Agrawal (2020), Physical Methods in Chemistry and Nano Science. Volume 5: Molecular and Solid State Structure (MiDAS Green Innovation, Limited).

[60] Laserna, JJ (2014), \An introduction to raman spectroscopy: introduction and basic principles," Raman/Infrared Spectroscopy.

[61] Long, Derek Albert (2002), \The raman e_ect: a uni_ed treatment of the theory of raman scattering by molecules," .

[62] McCreery, Richard L (2005), Raman spectroscopy for chemical analysis, Vol. 225 (John Wiley & Sons).

[63] Nandi, S. (2021). Raman spectroscopy [Preprint]. Indian Association for the Cultivation of Science.